Experimental and computational studies of turbulent separating internal flows

OLLE TÖRNBLOM

KTH Engineering Sciences

Doctoral Thesis in Fluid Mechanics
Stockholm, Sweden 2006

Experimental and computational studies of turbulent separating internal flows

by

Olle Törnblom

June 2006
Technical Report from
KTH Mechanics
SE-100 44 Stockholm, Sweden
ISBN 91-7178-416-0

Typsatt med pdfLaTeX och TeXShop.

Akademisk avhandling som med tillstånd av Kungliga Tekniska Högskolan i Stockholm framlägges till offentlig granskning för avläggande av teknologie doktorsexamen fredagen den 8 september 2006 kl 10.15 i Salongen på KTH-biblioteket, Osquars backe 31, Kungliga Tekniska Högskolan, Stockholm.
Opponent på avhandlingen är Professor Michel Stanislas från École Centrale de Lille.

Universitetsservice US AB, Stockholm 2006

Experimental and computational studies of turbulent separating internal flows

Olle Törnblom 2006
KTH Mechanics
SE-100 44 Stockholm, Sweden

Abstract

The separating turbulent flow in a plane asymmetric diffuser with 8.5 degrees opening angle is investigated experimentally and computationally. The considered flow case is suitable for fundamental studies of separation, separation control and turbulence modelling. The flow case has been studied in a specially designed wind-tunnel under well controlled conditions. The average velocity and fluctuation fields have been mapped out with stereoscopic particle image velocimetry (PIV). Knowledge of all velocity components allows the study of several quantities of interest in turbulence modelling such as the turbulence kinetic energy, the turbulence anisotropy tensor and the turbulence production rate tensor. Pressures are measured through the diffuser. The measured data will form a reference database which can be used for evaluation of turbulence models and other computational investigations. Time-resolved stereoscopic PIV is used in an investigation of turbulence structures in the flow and their temporal evolution. A comparative study is made where the measured turbulence data are used to evaluate an explicit algebraic Reynolds stress turbulence model (EARSM). A discussion regarding the underlying reasons for the discrepancies found between the experimental and the model results is made. A model for investigations of separation suppression by means of vortex generating devices is presented together with results from the model in the plane asymmetric diffuser geometry. A short article on the importance of negative production-rates of turbulent kinetic energy for the reverse flow region in separated flows is presented. A detailed description of the experimental setup and PIV measurement procedures is given in a technical report.

Descriptors: Fluid mechanics, turbulence, flow separation, turbulence modelling, asymmetric diffuser, boundary layer, PIV, vortex generator, separation control.

Preface

This thesis is an experimental and computational study of turbulent separating flow and its control. The thesis is based on and contains the following articles.

Paper 1. Törnblom O., Lindgren, B. & Johansson, A. V. 2006 Measurements of mean flow statistics in a plane asymmetric diffuser with 8.5° opening angle. To be submitted.

Paper 2. Törnblom O. & Johansson, A. V. 2006 Structural and temporal characteristics of the flow in a plane asymmetric diffuser with 8.5° opening angle. To be submitted.

Paper 3. Törnblom O, & Johansson, A. V. 2006 A Reynolds stress closure description of separation control with vortex generators in a plane asymmetric diffuser. Under consideration for publication in Physics of Fluids.

Paper 4. Gullman-Strand, J., Törnblom, O., Lindgren, B., Amberg, G. & Johansson, A. V. 2004 Numerical and experimental study of separated flow in a plane asymmetric diffuser. *Int. J. of Heat and Fluid Flow* **25**, 451–460.

Paper 5. Törnblom O. & Johansson, A. V. 2006 A note on the influence of negative turbulence production on separating flows. To be submitted.

Paper 6. Törnblom O., Lindgren, B. & Johansson, A. V. 2006 Experimental procedures for the investigation of the turbulent flow in a plane asymmetric diffuser by means of stereoscopic high-speed PIV. Technical report.

Division of work between paper authors

The papers included in this thesis have been written in collaboration with other researchers. Below follows a description of the contribution the respondent made to the different papers. Arne V. Johansson acted as supervisor and project leader in all investigations. The respondent made a major part of the writing of the papers, if not otherwise stated below. If parts of the work contained in the article have been presented elsewhere this is also stated.

Paper 1. Early stages of this work were made in collaboration with Björn Lindgren. The stereoscopic PIV measurements were performed by the respondent alone. Minor parts of the early work was presented at the 9th European Turbulence Conference, Southampton, UK, 2002 by the respondent, at the 11th International symposium on application of laser techniques to fluid mechanics, Lisbon, Portugal, 2002 by Björn Lindgren and at the 3rd International Symposium on Turbulence and Shear Flow Phenomena, Sendai, Japan, 2003 by the respondent, with written contributions to the conference proceedings.

Paper 2. The experimental work and data evaluation was done by the respondent.

Paper 3. The theory for the model, the implementation in the computational code and the computations were done by the respondent. Minor parts of the work has been presented at the 5th Symposium on Smart Control of Turbulence, Tokyo, Japan, 2004 by Arne V. Johansson, with written contributions to the conference proceedings.

Paper 4. The article is a blend of two separate written contributions to the 3rd International Symposium on Turbulence and Shear Flow Phenomena in Sendai, Japan, 2003, with the respondent and Johan Gullman-Strand as first authors. The experimental results were a joint work of the respondent and Björn Lindgren and the computations were done by Johan Gullman-Strand. The writing was done both by the respondent and Johan Gullman-Strand. Gustav Amberg and Arne V. Johansson acted as supervisors.

Paper 5. The data evaluation was done by the respondent.

Paper 6. The design, construction and testing of the diffuser wind-tunnel was done on equal terms by Björn Lindgren and the respondent. The PIV setup was done by the respondent alone.

Contents

Preface v
Division of work between paper authors vi

Chapter 1. Introduction 1

Chapter 2. Basic concepts 5
2.1. Governing equations 5
2.2. Turbulence modelling 6
2.3. Turbulent separation 8
2.4. Experimental techniques 13

Chapter 3. Results 16
3.1. Experiments 16
3.2. Turbulence modelling 19
3.3. Separation control model 21
3.4. Negative production in the reattachment zone 24

Chapter 4. Concluding remarks and outlook 26

Acknowledgments 28

Bibliography 29

Papers

Paper 1. Measurements of mean flow statistics in a plane asymmetric diffuser with 8.5° opening angle 37

Paper 2. Structural and temporal characteristics of the flow in a plane asymmetric diffuser with 8.5° opening angle 73

Paper 3. A Reynolds stress closure description of separation control with vortex generators in a plane asymmetric diffuser 93

Paper 4. Numerical and experimental study of separated flow in a plane asymmetric diffuser 123

Paper 5. A note on the influence of negative turbulence production on separating flows 143

Paper 6. Experimental procedures for the investigation of the turbulent flow in a plane asymmetric diffuser by means of stereoscopic high-speed PIV 155

CHAPTER 1

Introduction

Fluid flow is omnipresent in the world we inhabit. This is good for us, because it is hard to imagine life in an all solid world. For example, we all rely on the flow of two fluids, air and blood, for the life essential transportation of oxygen from the atmosphere to our cells. Some people may disagree on calling air a fluid, but from a physics point of view fluids include gases, liquids and plasmas. These have in common the ability to flow and the inability carry static shear loads.

Most flows that we encounter in our macroscopic world are turbulent. Also the airflow down to our lungs and the blood-flow in our aortae may be turbulent. Turbulence arises due to the nonlinear behaviour of flowing fluids, which makes small disturbances grow. The degree of nonlinearity is determined by a parameter called the *Reynolds number* that describes the ratio between the nonlinear inertia forces and the, disturbance damping, viscous forces. Turbulence arises at large Reynolds numbers and the number is named in honour of the British engineer Osborne Reynolds, who in the early 1880s was the first to show the relevance of this ratio for the onset of turbulence (Rott 1990).

Turbulent flow is characterised by irregular and three-dimensional motion of the fluid on a wide range of scales both in space and time. This is demonstrated in figure 1.1 showing a plume of smoke from a volcanic eruption. We can see that the Reynolds number of the plume is large from the wide range of scales present in the photograph. This is because the ratio of the largest and the smallest length scales of a turbulent flow is proportional to $Re^{3/4}$, where Re is a Reynolds number based on the large turbulent scales. The above relation was derived on by the Russian mathematician Andrej Kolmogorov in the early 1940s. The derivation is rather simple and is made on dimensional grounds, but it is based on a very important concept in our present understanding of turbulence, the spectral energy cascade. The basic idea of the energy cascade concept is that the kinetic energy of the turbulent motions is successively transferred from the larger eddies to smaller until viscous dissipation (or internal friction) transforms the kinetic energy into heat. We can then say, a bit simplified, that increasing the energy in the large scale turbulence (increasing the Reynolds number) will allow the kinetic energy to cascade down to even smaller scales before the viscosity is able to damp it out.

FIGURE 1.1. Mt. St. Helens, May 18, 1980. Photograph by Austin Post, USGS.

The above described property of turbulence, that the range of scales increases with the Reynolds number, is what makes makes accurate predictions turbulent flows so complicated. The computational effort needed to resolve a turbulent flow grows very rapidly with increasing Reynolds number, it is proportional to $Re^{11/4}$ (the required spatial resolution increases in each dimension as $Re^{3/4}$ and the required temporal resolution is proportional to $Re^{1/2}$). As an example Moin & Kim (1997) writes that with a supercomputer capable of 10^{12} floating point operations per second (1 teraflops) it would take several thousand years to make a computation that simulates the flow over a transport aeroplane for one second of flight time. That statement was written nearly ten years ago, before the first teraflop computer, today the fastest computer is capable of approximately 300 teraflops, but even with this terrific computer the simulation would still require nearly a decade of computational time.

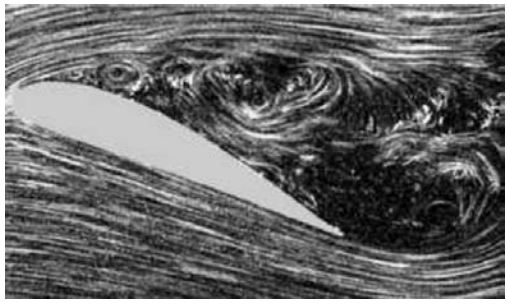

FIGURE 1.2. Flow separation on a wing at high angle of attack.

Spending years of computational time for one second of real time flow over an aeroplane is difficult to motivate. In aeronautics as well as in all other engineering fields that include flow at large Reynolds numbers, other methods have to be used for the evaluation and development of new designs. A natural and traditional way is to use experimental testing to learn about a flow or evaluate a design. Preliminary designs of aeroplanes or cars are often tested using down-scaled models in a wind-tunnel. However, it is not in all cases, economically or physically, feasible to do experimental testing and in those situations the common approach is to use some sort of model for the turbulence in order to circumvent the problem with insurmountable computational times. Much of the engineering turbulence research today is motivated by the need to gain knowledge that can be used to improve modelling predictions.

Shearing (or straining) is a necessary ingredient for disturbance growth and for turbulence to occur and be sustained. A fluid in relative motion to a solid object forms a boundary layer in which the relative velocity between the fluid and the solid is gradually decreased until it is zero at the surface of the solid object. The velocity gradient in a boundary layer causes a shearing of the fluid and boundary layers are thus likely to be turbulent if the Reynolds number is large.

The subject of the present thesis is separating flows. Separation occurs when the flow in the boundary layer next to a solid surface is slowed down and eventually reversed, forming a region of circulating flow between the surface and the outer flow. Figure 1.2 shows a typical example of flow separation, the stall of an aerofoil at high angle of attack. Other situations where separation might occur are the rear end cars and trucks where it leads to increased air resistance and fuel consumption. In ventilation systems the large scale fluctuations of a separation can result in noise and decreased performance. In fact, there are countless number of applications where internal flow separation can be of importance since the phenomenon is quite likely to occur wherever a pipe,

channel or duct that is used to transport a fluid is subject to a change in geometry or direction.

CHAPTER 2

Basic concepts

2.1. Governing equations

The motions of liquids or gases, which are both fluids, are always consequences of a large number of discrete interactions between the molecules of the fluid. The ways in which the molecules interact determine the bulk properties of the fluid, such as the density, viscosity, heat-transfer coefficient, heat-capacity etc. In many cases it is not necessary to consider the interactions of individual molecules but instead regard the fluid as a continuum. This is what one usually does in fluid mechanics and what will be done in the remaining parts of this thesis.

The flow considered in this thesis and many other flows at moderate speeds can be described by the incompressible Navier-Stokes equations,

$$\rho\left(\frac{\partial \tilde{u}_i}{\partial t} + \tilde{u}_j\frac{\partial \tilde{u}_i}{\partial x_j}\right) = -\frac{\partial \tilde{p}}{\partial x_i} + \frac{\partial}{\partial x_j}\left(\mu\frac{\partial \tilde{u}_i}{\partial x_j}\right) \tag{2.1}$$

$$\frac{\partial \tilde{u}_i}{\partial x_i} = 0. \tag{2.2}$$

Cartesian tensor notation has been used when the above equations were formulated and Einstein's summation convention should be applied when the tensorial expression is expanded. The velocity tensor $\tilde{u}_i$ is of first rank and contains the velocities corresponding to the three spatial directions x_i, the scalar $\tilde{p}$ is the pressure and ρ and μ are constants for the density and dynamic viscosity, respectively. The Navier-Stokes equations can be derived by using Newton's second law of motion to relate the change of momentum of an infinitesimal volume of fluid to the forces acting on the same volume. The forces acting in the normal directions on the sides of the control volume can be identified as pressure and give rise to the first term in the right hand side of equation 2.1. Shearing of the fluid give rise to forces that are tangential to the sides of the control volume. If the tangential forces are linearly proportional to the rate of the shearing the fluid is said to be Newtonian. Two of our most common fluids, air and water, have this behaviour. Therefore, much of the fluid mechanics research, including the present work, is concentrated on Newtonian fluids. Viscosity is the property of the fluid that determines how large the tangential force on the control volume sides will be for a given rate of shear,

this property is thus a constant in isothermal Newtonian fluids. Equation 2.2 is called the continuity equation and describes the conservation of mass in an incompressible fluid.

When analysing turbulent flows, it is often useful to make a decomposition of the velocity and pressure fields into a mean part and a fluctuating part,

$$\tilde{u}_i = U_i + u_i, \tag{2.3}$$

$$\tilde{p} = P + p, \tag{2.4}$$

this is often called Reynolds decomposition. Here capital letter quantities are ensemble averages and lower-case letters represent fluctuations. Taking the ensemble average of equations 2.1 and 2.2 yields the following equations for the mean flow,

$$\rho\left(\frac{\partial U_i}{\partial t} + U_j\frac{\partial U_i}{\partial x_j}\right) = -\frac{\partial P}{\partial x_i} + \frac{\partial}{\partial x_j}\left(\mu\frac{\partial U_i}{\partial x_j} - \rho\overline{u_i u_j}\right) \tag{2.5}$$

$$\frac{\partial U_i}{\partial x_i} = 0. \tag{2.6}$$

These equations are called the Reynolds equations or Reynolds averaged Navier-Stokes (RANS) equations and are the equations that are solved in turbulence model computations. Note the last term in equation 2.5, which is a derivative of the Reynolds stress tensor $-\rho\overline{u_i u_j}$. The overline is used to indicate that it is an ensemble average. The Reynolds stress appears in the equations for the mean velocity as an unknown extra stress caused by the turbulent fluctuations. The objective of RANS turbulence models is to predict this terms, as accurately as possible, from a limited amount of flow information. Modelling is needed since equations 2.5 and 2.6 only constitute four equations but the number of unknowns are ten (six unknowns in the Reynolds stress tensor due to index symmetry). This is called the closure problem of turbulence modelling.

2.2. Turbulence modelling

Historically, most turbulence models have been based on the concept of a turbulent viscosity or eddy-viscosity. This concept make use of the notion that the momentum transfer in a turbulent flow is dominated by the motion of the large energetic turbulent eddies. In 1877, the same era Osborne Reynolds did his famous pipe-flow experiment in, Joseph Boussinesq suggested that the effects of the turbulent motion in a boundary-layer type of flow could be described by an additional turbulent viscosity. This basic idea is expressed in the generalised Boussinesq hypothesis as

$$a_{ij} = -2\frac{\nu_T}{K}S_{ij}, \tag{2.7}$$

which says that the Reynolds stress anisotropy

$$a_{ij} \equiv \frac{\overline{u_i u_j}}{K} - \frac{2}{3}\delta_{ij} \tag{2.8}$$

is linearly proportional to the strain rate tensor of the mean flow

$$S_{ij} \equiv \frac{1}{2}\left(\frac{\partial U_i}{\partial x_j} + \frac{\partial U_j}{\partial x_i}\right). \tag{2.9}$$

K is the turbulent kinetic energy defined as $\overline{u_i u_i}/2$.

The simplest turbulence models describes the turbulent viscosity, ν_T, explicitly in mean flow quantities, the next level of modelling is to introduce *one* extra transport equation *e.g.* for the turbulent viscosity as in the Spalart-Allmaras model. These types of models can often perform quite well in well defined flows and are typically used in aeronautics. However, if a model should be able to give reasonable predictions in a wide range of flows, at least two transport equations are needed, by which a turbulence length-scale and a turbulent velocity-scale and hence a turbulent viscosity can be deduced. A large majority of the turbulence models used in engineering applications today can be categorised as two-equation models.

In practically all two-equation models a transport equation for the turbulent kinetic energy, K, is used in order to get a turbulence velocity scale. Then if $K^{1/2}$ is used as a measure of the turbulent velocity scale the turbulent viscosity can be expressed as

$$\nu_T \propto K^m Z^n, \tag{2.10}$$

where Z is the auxiliary 'length scale determining quantity'. A common choice for Z is the turbulence dissipation rate, ε, (giving m=2, n=-1) (Chou 1945) but other quantities such as the inverse of the turbulence time-scale (ω=ε/K, m=1, n=-1) (Kolmogorov 1942; Wilcox 1988) or the turbulence time-scale (τ=K/ε, m=1, n=1) are also used.

Models based on the Boussinesq hypothesis usually performs reasonably well in flows where a single component of the Reynolds stress tensor is of significant importance, such as attached boundary-layer flows. However, in more complex flows and flows where effects of rotation are important the eddy-viscosity assumption will fail and more elaborate models have to be used. The natural next step, if an eddy-viscosity model fails, is to use a set of transport equations for the components of the Reynolds stress tensor (6 equations) plus one for the 'length scale determining quantity' (see *e.g* Launder *et al.* 1975; Sjögren & Johansson 2000). Such models, called differential Reynolds stress models (DRSM), will in a natural way include history effects for the individual Reynolds stresses and rotational effects on the turbulence. However, the increased computational cost and complicated near-wall modelling have prevented DRSMs from becoming widely used.

An intermediate type of models, that capture more of the turbulence physics than eddy-viscosity models but still only need two transport equations for turbulence quantities, is the family of explicit algebraic Reynolds stress models (EARSM) (see *e.g* Speziale *et al.* 1991; Wallin & Johansson 2000).

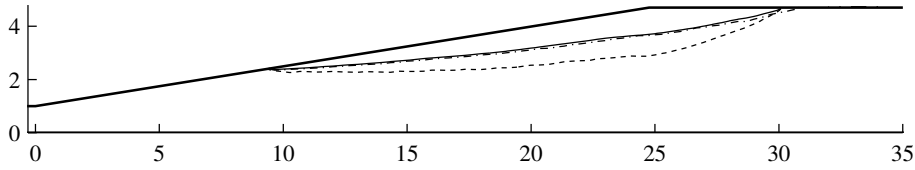

FIGURE 2.1. Comparison between different definitions of the separation bubble; dividing streamline (- - -), zero streamwise mean velocity (—) and backflow 50% of the time ($- \cdot -$).

An EARSM uses an explicit relation between the Reynolds stress anisotropy and the mean strain and rotation rate tensors. The explicit relation is derived from the transport equations for the Reynolds stress anisotropy after having dropped the advection and diffusion terms under the assumption that the anisotropy varies slowly in space and time.

A fundamentally different approach to turbulence modelling is large eddy simulations (LES) where the large scale turbulent motions are resolved and a model is used to account for the effects of the smaller scales. LES can be expected to capture more of the flow physics as compared to single point closures at the price of an increased computational effort.

Solving the Navier-Stokes equations without any model is often called direct numerical simulation (DNS). This is an accurate but very computationally expensive approach that is limited to flows at relatively small Reynolds numbers.

2.3. Turbulent separation

Separating flows can in general be divided into two main categories depending on the cause of the separation, the two categories are here denoted *geometry induced* and *pressure-gradient induced* separation. In a geometry induced separation a recirculating region forms due to the presence of a sharp edge, for example a corner. The flow is unable to follow the shape of the surface since that would involve extreme acceleration of the flow. A pressure gradient induced separation is a gradual process that occurs in decelerating flows.

2.3.1. *Definition of the separated region*

Turbulent boundary-layer separation is, in contrary to most laminar separations, a non-stationary phenomenon and the location of the point on the wall where backflow first occurs will fluctuate. The combination of energetic turbulent motions with large spatial scales and a mean flow with low velocities makes the instantaneous flow appear very different from the mean. The most common definition of the separation point is that it is the location where the mean wall shear stress is zero but this measure does not tell us anything about

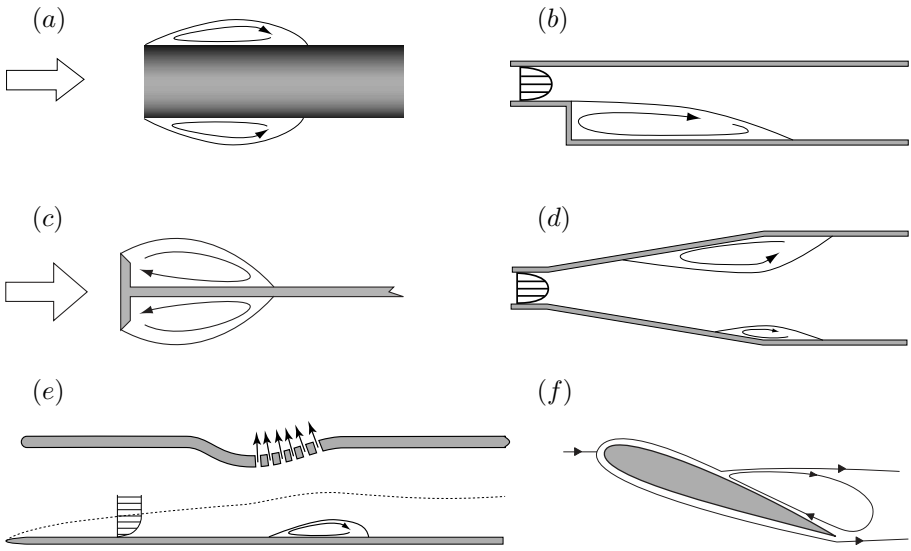

FIGURE 2.2. Typical geometries for flow separation.

where instantaneous separation may occur. However, the backflow coefficient, χ, defined as the fraction of time that the flow is reversed does tell us something about the separation point movement. Simpson *et al.* (1981*a*) use the term *incipient detachment point* to denote the position where χ=0.01 and defined the detachment point as the point where χ=0.5. Most investigations indicate that χ=0.5 coincide with the point of vanishing wall shear stress (Simpson 1989).

I have found no firm definition of the term *separation bubble* in the literature. I have encountered three different definitions or interpretations for the limits of a separation bubble: (*i*) the separation bubble is the mean recirculating region within the dividing streamline (also called separation streamline) reaching between the stagnation points on the wall at the separation and reattachment points, (*ii*) the separation bubble is the region with mean backflow *i.e.* below the curve of zero mean velocity and (*iii*) the separation bubble is the region with backflow more than 50% of the time ($\chi = 0.5$). The differences between these three definitions are illustrated in figure 2.1. In the present thesis the first definition will be used. This seems also as the most established one in the literature.

2.3.2. *Typical flow configurations*

A few typical flow configurations used in fundamental studies of separating flows are depicted in figure 2.2.

Figure 2.2*a* shows the geometry induced separation on a blunt edge, the edge can be either the front end of a cylinder or a flat plate. This type of flow has been investigated experimentally by *e.g.* Cherry *et al.* (1984), Kiya & Sasaki (1983, 1985) and Sigurdson (1995).

The backward-facing step flow depicted in figure 2.2*b* has been the subject of a multitude of investigations, the inlet flow is usually either a channel flow or a boundary-layer with a free-stream. Experimental investigations of the flow over a backward-facing step are *e.g.* Etheridge & Kemp (1978), Armaly *et al.* (1983), Jovic & Driver (1994, 1995), Kasagi & Matsunaga (1995) and Yoshioka *et al.* (2001*a*,*b*). The flow-case has also been investigated in a direct numerical simulation by Le *et al.* (1997).

Another frequently studied geometry induced separation is that behind a fence or flow-normal plate, shown in figure 2.2*c*. This type of flow was used in the investigations by Ruderich & Fernholz (1975), Castro & Haque (1987) and Hancock (1999, 2000).

Investigations of pressure gradient induced separation are not quite as common as those where the separation occurs on a sharp edge. Naturally, also this category of separating flows allows for a variety of experimental configurations. Figure 2.2*d* shows one of many conceivable configurations for internal flow separation, or diffuser separation studies. The present thesis deals with a flow falling under the diffuser category, so the literature related to plane asymmetric diffusers is omitted here and described in more detail in section 3.1. Examples of studies of separating diffuser flow in other geometries are Yin & Yu (1993) and Brunet *et al.* (1997).

Flows of the kind illustrated by figure 2.2*e*, where a boundary-layer under a free-stream is forced to separate and reattach on a plane wall, are found in several investigations *e.g.* Perry & Fairlie (1975), Dianat & Castro (1991) and Angele (2003); Angele & Muhammad-Klingmann (2005). Comparable axisymmetric geometries are also used in some investigations *e.g.* Dengel & Fernholz (1990) and Alving & Fernholz (1995, 1996). I include also in this category flows with a free-stream and pressure gradient induced separation and reattachment on smoothly curved walls such as the ones used in the investigations of Stratford (1959) and Song *et al.* (2000); Song & Eaton (2002*a*, 2004*b*,*a*). Direct numerical simulations of boundary-layer separation on plane walls have been made by for example Spalart & Coleman (1997), Na & Moin (1998) and Skote & Henningson (2002).

Flows with open, 'aerofoil-like', separations, as the one illustrated in figure 2.2*f*, have a natural connection to aerospace application and have been covered in several studies. Most notable is perhaps the series of articles by Simpson and co-workers (Simpson *et al.* 1981*a*,*b*; Shiloh *et al.* 1981).

2.3.3. *The boundary-layer flow before separation*

Boundary-layer separation on a smooth surface occurs if the boundary-layer is subjected to a strong enough adverse pressure gradient (APG) and if the duration of the APG is long enough. APG boundary-layers grow more rapidly than for instance zero pressure gradient (ZPG) boundary-layers since an APG is associated with a deceleration of the external flow and we get from the continuity equation (equation 2.6) that the wall normal velocity component V will depend on the deceleration of the streamwise velocity U as

$$V(x,y) = -\int_0^y \frac{\partial U(x,y')}{\partial x}\mathrm{d}y', \tag{2.11}$$

in a two-dimensional flow where $W = 0$. The boundary layer will hence grow not only due to momentum diffusion, as in the ZPG case. If the APG is sustained, the velocity in the near-wall region will continue to decelerate and eventually reverse and form a separated region. Turbulent boundary layers can sustain adverse pressure gradients longer than laminar ones due to the increased momentum diffusion caused by the turbulence that more efficiently brings down high-velocity fluid towards the wall.

Another important feature of APG boundary-layers is that the velocity profiles must have an inflection point. This is readily seen if we consider equation 2.5 evaluated at the wall[1],

$$\frac{1}{\rho}\frac{\partial P}{\partial x} = \nu\frac{\partial^2 U_1}{\partial y^2}\bigg|_{y=0}. \tag{2.12}$$

Since $\partial P/\partial x$ is positive when we have an adverse pressure gradient $\partial^2 U/\partial y^2|_{y=0}$ must also be positive. But at the outer edge of the boundary-layer $\partial^2 U/\partial y^2$ must be negative, thus the velocity profile must have an inflection point somewhere between the wall and the outer edge. This inflection point will of course coincide with the point of maximum shear in the boundary-layer. With a sustained pressure gradient the inflection point will move further out from the wall according to equation 2.11 and moving with it is also the position of maximum Reynolds shear stress, $-\rho\overline{uv}$, since the turbulence production will have its maximum near the inflection point (see *e.g.* Alving & Fernholz 1996). As the peak in $-\rho\overline{uv}$ moves away from the wall the momentum transfer to the near-wall region will diminish and thus facilitate reversal of the near-wall mean flow. The turbulence production ($-\overline{u_i u_j}\partial U_i/\partial x_j$) in adverse pressure gradient boundary-layers may, in contrast to the turbulence production in zero pressure gradient boundary-layers, have quite large contributions from the normal Reynolds stresses due to the decelerating flow in the streamwise direction (Alving & Fernholz 1996; Simpson *et al.* 1981*a*). Alving & Fernholz suggest also that the

[1]Note that $\frac{\partial\overline{uv}}{\partial y}\Big|_{y=0} = \frac{\partial\overline{vv}}{\partial y}\Big|_{y=0} = 0$.

reduced shear rates in an APG boundary-layers may decrease the dissipation rate of turbulence due to reduced vortex stretching.

2.3.4. *Motions of the separated region*

For geometry induced separations several authors have reported a low frequency motion where the reattachment point moves back and forth in a quasi-periodic manner (see *e.g.* Kiya & Sasaki 1985; Le *et al.* 1997). In pressure gradient induced separations this type of motion appears to be less organised and no reports of motion at distinct frequencies have been found. However, motions on low frequencies, or wavenumbers, do exist and they are highly energetic but they are spread out evenly in the spectrum (Buice & Eaton 1997). One can speculate that the static separation point in the geometry induced separations gives a more stationary shear layer in which the quasi-periodic motions can appear, and conversely that the constantly changing upstream condition of a pressure induced separation hinders the onset of any periodic motion of the reattachment point. In fact, thinking about the separated region as a coherent region stretching between the separation and reattachment points is a mistake for most flows with pressure gradient induced separation. The PIV velocity fields of the present investigation clearly show that the region of mean backflow is caused by instantaneous backflow in smaller regions often with regions of forward flow in between. The same behaviour is observed in Angele & Muhammad-Klingmann (2005)

2.3.5. *Reattachment region*

It is well known that the Reynolds stresses decreases rapidly in the downstream direction in the region where reattachment occurs while most other flow quantities undergo changes at a considerably lower rate. Bradshaw & Wong (1972) suggested in an early investigation that the large eddies from the shear-layer were torn apart at reattachment and that one part was convected 'upstream' by the backflow and the other downstream. The size of the vortices would thus be approximately halved. Later investigations have however shown that the sizes of the large scale vortices are similar before and after reattachment.

Song & Eaton (2002*b*) hypothesise that the positive streamwise velocity gradient, $\partial U/\partial x$, stretch the streamwise vortices so that $\overline{vv}$ and $\overline{ww}$ increase while $\overline{uu}$ is decreased. But they also say that this would successively lead to a redistribution of energy from $\overline{vv}$ to $\overline{ww}$ and back to $\overline{uu}$ due to the presence of the wall or that the energy is dissipated.

In conclusion it may be said that there are still some important open questions remaining to be answered regarding the reattachment flow.

2.3.6. *Boundary layer recovery after reattachment*

After reattachment a new boundary-layer starts to develop on the wall, the circumstances under which it forms are however rather unusual since large scale turbulence created at the separation is continuously supplied from upstream. Many investigations (*e.g.* Bradshaw & Wong 1972) report a scenario where a new boundary layer, following the logarithmic law, grows out from the surface under influence of the turbulence from the separation. The turbulence quantities generally recover more slowly than the mean velocities.

2.4. Experimental techniques

The present thesis is mainly based on experimental work. It can be seen from the Navier-Stokes equations (2.1) that the important variables in an incompressible flow are the velocity vector and the pressure. Balancing equation 2.1 in a turbulent flow requires simultaneous measurements of the velocity vectors (knowing all velocities, it is not necessary to measure the pressure in an incompressible flow) in a volume with a spatial and temporal resolution fine enough to resolve the smallest scales of the flow. This is usually not possible in practise, and perhaps not even desired in many cases due to the enormous amount of data such measurements would produce. Instead a common approach in turbulence research is to measure the statistical properties of the flow. Hence the equations subject to balancing are the RANS equations rather than the Navier-Stokes equations.

Measurement techniques applicable to separating flows are limited to methods that are able to determine both the magnitude and direction of the flow. This exclude the use of constant temperature hot-wire anemometry (CTA), an otherwise very common and accurate measurement technique for turbulent flows. In separating flows the traditional measurement methods are instead pulsed hot-wire anemometry (see *e.g.* Bradbury & Castro 1971) and laser Doppler velocimetry (LDV) (see *e.g.* Tropea 1995). Both these methods measures the velocity in a single point, or rather the spatial average velocity in a small volume. Such measurement methods have the advantage that a large number of samples can be collected without accumulating unwieldy amounts of data and thus facilitate averaging of a turbulent flow. Particle image velocimetry (PIV), a technique extensively used in the present thesis, is also able to determine both the magnitude and the direction of the flow (if cross-correlation PIV is used *cf.* section 2.4.1) and is thus, at least in that aspect, qualified as an appropriate tool for investigations of separating flows. PIV is, in contrast to pulsed hot-wires and LDV, a whole field technique that, in a plane of the flow, instantaneously measures the velocities at several locations. Getting whole field measurements of the flow is of course advantageous if spatial structures are of interest. Drawbacks of PIV are the large amounts of data

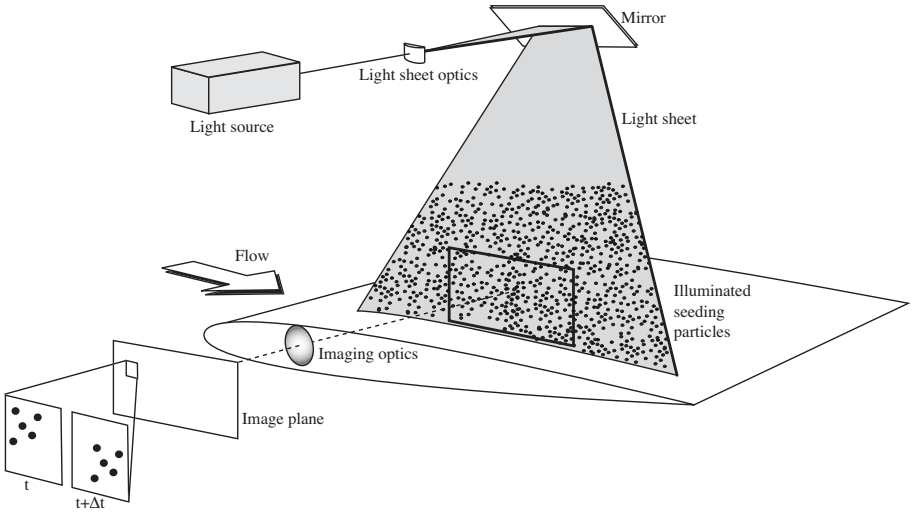

FIGURE 2.3. Sketch of a basic setup for particle image velocimetry.

that have to be processed and stored and the spatial averaging that may bias the measured turbulence levels.

2.4.1. *Particle image velocimetry*

Measuring the velocity of a moving fluid can be done in many different ways and the present thesis work is based mainly on measurements by particle image velocimetry. A sketch of a basic PIV-setup is shown in figure 2.3. In PIV, particles are used as indicators of the fluid motion, the particles are visualised by illuminating a plane of the flow with a light-sheet. Two consecutive images, separated by the time Δt are taken of the particle pattern. By analysing the displacement of the particle pattern between the images the velocity can be calculated. Introductions to the PIV technique are given in *e.g.* Westerweel (1993) and Raffel *et al.* (1997).

A pulsed laser is often used as light-source, the pulses typically have a duration that is smaller than 100 ns and can thus freeze the moving particle pattern. The two images of the particle pattern can either be recorded on two different frames or on the same frame by keeping the camera shutter open and flashing the light-source twice. The latter method is simpler to implement but has a directional ambiguity, which makes it unsuitable for separating flows. The measurement noise is also higher for double exposure PIV. The first method requires that the camera is able to record two individual frames within the time interval Δt, this usually requires special equipment if applied to flows with large velocities *e.g.* wind-tunnel flows. The advancements in digital image recording techniques during the last decade have made PIV a more versatile and

used measurement technique and digital PIV, *i.e.* PIV using digital cameras, is today the by far most used technique.

The common approach to determine the particle displacements between the two consecutive images is to divide the images into a number of smaller *interrogation areas* (IAs) *cf.* figure 2.3. Each IA is used to determine a velocity vector. The average particle displacement within an IA is determined by calculating a spatial correlation, in the case of a double exposed frame it will be an auto-correlation and if two frames are used it is a cross-correlation between the corresponding IAs of the two frames. The two methods are thus often called auto-correlation and cross-correlation PIV respectively. The location of the peak of the correlation function corresponds to the displacement that gives the best match of the particle patterns. The fastest and most common method to compute the correlations is to use discrete Fourier transforms.

Much of the PIV development have been in the methods and algorithms used to determine the particle displacement. Modern algorithms are usually iterative and begin by calculating a large-scale velocity field using large size IAs. The large scale field is then used in order to shift the interrogation areas in the consecutive iteration, this usually leads to a better signal to noise ratio and an increased dynamic range. The iterative process can be continued with smaller IAs until the average number of particles present in a IA becomes the limiting factor. Another method, used in conjunction with an iterative algorithm, is to deform the IAs in correspondence with the flow deformation. The interested reader is referred to *e.g.* Stanislas *et al.* (2005) for a review on modern PIV algorithms.

In planar PIV a single camera with its optical axis perpendicular to the light-sheet plane is used. With this method the two velocity components in the light-sheet plane are obtained, therefore this is sometimes called two-component (2C) PIV. In stereoscopic PIV two cameras are used to image the particles in the light sheet and at least one of the cameras has an optical axis not perpendicular to the light sheet plane. This makes it possible to determine the out of plane particle displacement from the displacements measured by the two cameras and a calibration function (see *e.g.* Scarano *et al.* 2005; Wieneke 2005). Stereoscopic PIV is hence sometimes also called three-component (3C) PIV.

CHAPTER 3

Results

3.1. Experiments

The papers 1, 2 and 6 of this thesis are directly related to experiments made in a plane asymmetric diffuser flow. The diffuser has an opening angle of 8.5° and the geometry of this flow-case is shown in figure 3.1. Upstream the diffuser is a long plane channel in which a fully developed turbulent channel flow is generated. Smooth radii are used in the transitions between the straight walls and the inclined in order not to introduce disturbances and avoid geometry induced separation at the upstream corner.

The flow in a 10° plane asymmetric diffusers has been studied experimentally earlier by Obi and co-workers, their investigations include LDV measurements of the mean flow and in-plane turbulence components, separation control and Reynolds number dependencies (Obi *et al.* 1993*a*,*b*, 1997, 1999). Another experimental investigation of the 10° diffuser was performed by Buice & Eaton (2000). Several turbulence model investigations have used the plane asymmetric diffuser as a reference case, see *e.g.* Obi *et al.* (1993*a*, 1999), Hellsten & Rautaheimo (1999), Apsley & Leschziner (1999), Gullman-Strand (2004) and Sveningsson (2006). Large eddy simulation (LES) was used to compute the diffuser flow in the investigations of Kaltenbach *et al.* (1999) and Wu *et al.* (2006) who studied the general flow characteristics and an internal layer forming on the non-separating side of the diffuser respectively. Herbst *et al.* (2006) made large eddy simulations of both the 8.5° and 10° diffuser, studying *e.g.* the Reynolds number dependence of the flow.

The motivation for designing an experiment with a smaller diffuser angle, as compared to the previous experiments, was to get a smaller separation that was expected to: facilitate keeping the flow two-dimensional, make the flow-case more challenging for turbulence models and be more sensitive to control with moderate actuation amplitudes.

Figure 3.2 shows profiles of the average U-velocity, the figure shows also the dividing streamline between the recirculating region and the outer flow. The flow is characterised by a jet-like high velocity region that follows the straight wall and low velocity region along the inclined wall. In between these two regions is a layer of strong shear. From $x/H \approx 6$ and downstream the

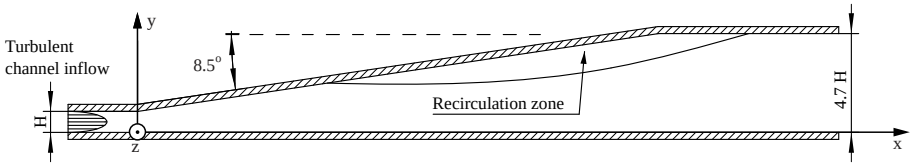

FIGURE 3.1. The plane asymmetric diffuser.

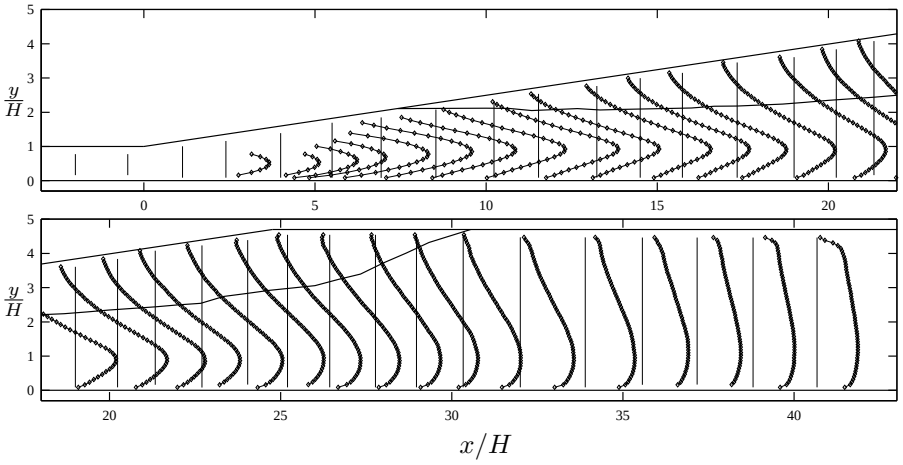

FIGURE 3.2. Profiles of mean streamwise velocity.

peaks of the U-velocity profiles stay at approximately the same distance from the straight wall, although the peaks are quite vague in the most downstream profiles. A relatively high peak velocity is maintained over the region in x where the separation bubble height is increasing because the effective diffuser angle is nearly zero here due to displacement from the recirculation region. The small decrease in peak velocity which is yet seen in this region is mainly due to a spreading of the peak that most likely can be attributed to turbulent diffusion.

There are easily recognisable inflection points on the low velocity side of the profiles but less pronounced inflection points are also found on the straight wall side of the velocity peak in a region between $x/H{\approx}5$ and 10. The inflectional profile on the low velocity side of the diffuser eventually leads to a recirculating region with flow reversal near the inclined wall. The recirculation region, indicated with a solid line in figure 3.2, starts at $x/H{=}7.4$ and extends to $x/H{\approx}30.5$. A maximum backflow velocity of approximately $0.1U_b$ is found around $x/H{=}21$. After reattachment there is a slow development of the profiles towards a symmetric shape although the most downstream of the presented profiles is still asymmetric.

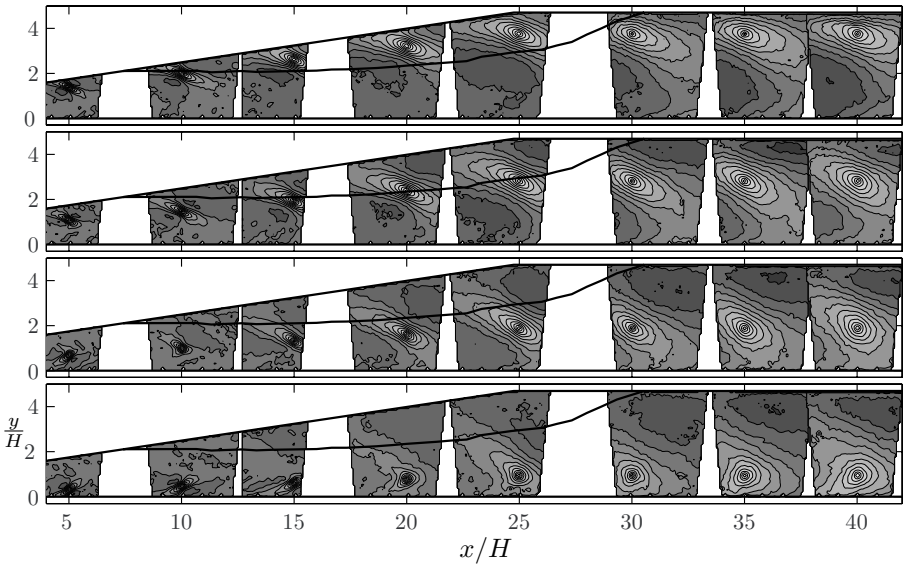

FIGURE 3.3. Auto-correlation functions for the spanwise velocity component at x_0/H =5, 10, 15, 20, 25, 30, 35, 40 and $y_0/h(x)$ =0.2, 0.4, 0.6, 0.8 where $h(x)$ is the local height.

The wide and strong shear-layer below the backflow region in figure 3.2 is the major producer of turbulence energy as it interacts with the incoming turbulence from the channel flow. All the non-zero components in the Reynolds stress tensor, ($\overline{uu}$, $\overline{vv}$, $\overline{ww}$ and $\overline{uv}$) have their maxima within this shear-layer.

The peaks of the auto-correlation functions

$$R_{ww}(x,y) = \frac{\overline{w(x_0,y_0)w(x,y)}}{\sqrt{\overline{ww}(x_0,y_0)\overline{ww}(x,y)}}, \tag{3.13}$$

shown in figure 3.3, have a pronounced inclined shape, bearing large resemblance with structures frequently seen in instantaneous realisations of the flow. These inclined structures of spanwise fluctuations have been observed to come in pairs of one positive and one negative structure and negative correlations are indeed found on both sides of the auto-correlation peaks along the minor axes of the peaks. This shape of the correlations can be interpreted as an indication of frequent appearance of large scale vortices with their axes inclined approximately 45° relative to the main flow direction. Horseshoe-like, or hairpin-like vortices are known to appear frequently in turbulent boundary-layers and are described in for example Head & Bandyopadhyay (1981), Robinson (1991), Adrian *et al.* (2000) and Carlier & Stanislas (2005). The observed structures could be interpreted as the legs of hairpin vortices, this is also supported, in paper 2, by a temporal sequence of instantaneous velocity fields. The sequence

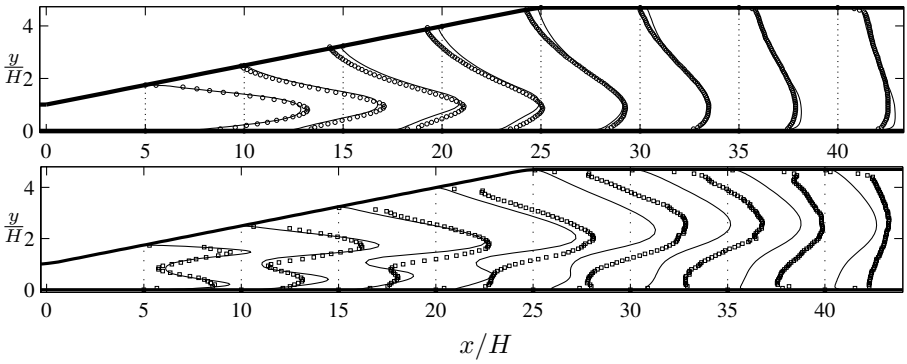

FIGURE 3.4. Comparison between an EARSM computation and experimental data. The top figure compares the streamwise mean velocity and the bottom figure the turbulent kinetic energy.

shows how one of the above described structures (supposedly) moves in the spanwise direction out of the measurement plane followed by the appearance of a typical hairpin vortex head. Studies of structures of the spanwise velocity fluctuations in an xy-plane are surprisingly few so I have not found any investigation discussing these structures and particularly not in conjunction to hairpin or horseshoe vortices. An increased backflow rate was observed as a possible consequence of the ejection from a hairpin vortex, but many aspects of the importance of these structures for the backflow region remains to be revealed.

3.2. Turbulence modelling

Papers 3 and 4 in this thesis involve turbulence model based computations of the flow in the plane asymmetric diffuser. In paper 3 a differential Reynolds stress model (DRSM) is applied to the 8.5° diffuser-flow and in paper 4 the predictions of an explicit algebraic Reynolds stress model (EARSM) are compared to experimental data in both the 8.5° and the 10° diffuser flow.

Making accurate predictions of the plane asymmetric diffuser flow is an extremely difficult task and the turbulence models of today have to evolve further before satisfactory results can be achieved. The diffuser flow is characterised by rapid changes of the mean flow, first at the diffuser inlet a sudden retardation and turning of the flow occurs, then in the flow through the diffuser the mean flow profiles are continuously changing and finally after reattachment the gradients of the mean flow are rapidly diminished. All these rapid changes make history effects of the turbulence important since turbulence produced in one location will immediately be advected to a new location where the circumstances are different. Different levels of modelling are, to different degrees able

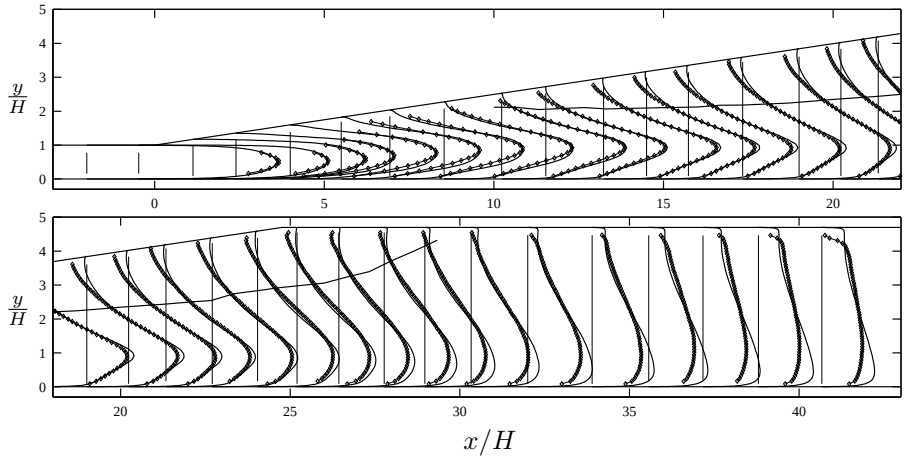

FIGURE 3.5. Mean streamwise velocity profiles from the DRSM computation (solid lines) and the experiment (symbols). The dividing streamline from the experimental data is also included.

to capture history related features. A DRSM can capture the advection and diffusion of Reynolds stress anisotropy while this is not possible in a two-equation model. Therefore it is especially interesting to see how an EARSM can predict this flow, where the advection and diffusion of anisotropy are neglected (in a chosen frame of reference) under an assumption of weak equilibrium implying that the anisotropy variations should be slow in space and time (see *e.g.* Wallin & Johansson 2000, 2002).

Figure 3.4 compares the EARSM predictions of mean streamwise velocity and turbulent kinetic energy with the experimental data. In comparison with many other models tested in the diffuser (see Hellsten & Rautaheimo 1999) the agreement with experimental data of the present EARSM results can be considered as good. However, the EARSM solution is not totally satisfactory. The most striking difference in the mean flow is perhaps the smaller reverse flow velocity seen in the EARSM solution, this is a problem common to nearly all turbulence models and paper 5 in this thesis give some ideas to the reason behind this. The decreased backflow, results in a reduced size of the separation bubble, which affects the whole flow field. Therefore it is difficult to draw conclusions regarding the reasons behind the underestimated levels of turbulent kinetic energy also shown in figure 3.4 but a hypothesis put forward in paper 4 is that the dissipation rate is overestimated in the EARSM. The overestimated dissipation rate can be interpreted as an underestimation of the turbulence integral length-scale, a quantity that appears to be relatively large and grow fast in the real flow judging from the correlations in paper 2. The predicted

separation size for the EARSM was in better agreement with the experimental data (from Buice & Eaton 1997) for the 10° case. This support the idea that the 8.5° diffuser is an even more challenging test for turbulence models due to the weaker pressure gradient.

In paper 3 a differential Reynolds stress model is used, the model uses a recalibrated version of the linear pressure strain rate model presented by Launder *et al.* (1975). A modified elliptic blending model (see *e.g.* Manceau 2005) is used for the near wall treatment of the Reynolds stress equations. The inverse turbulence timescale, ω, is used as the auxiliary length-scale determining quantity, the modelling of this equation is essentially the same as that of Wilcox (1994), including the low Reynolds number treatment.

The differential Reynolds stress model gives a good agreement with the experimental data outside the separation from the inlet and down to roughly x/H=25 (see figure 3.5), where the velocity peak in the computation is starting to move towards the straight wall while the experiment shows a velocity peak at an approximately constant distance from the straight wall. After reattachment the gradients of the experimental profiles are reduced faster in the streamwise direction as compared to the computation. This indicates that the DRSM as well as the EARSM has problems with predicting the turbulent length-scales of the flow correctly and thus do not predict the turbulent diffusion correct either. This in not surprising since the two models use the same ω-model to determine the turbulence length-scale. However, it is not believed that simply switching to another length-scale determining quantity will solve this problem. The largest discrepancies between the DRSM solution and the experiment are seen in the separated region where the predicted strength of the backflow is too small.

The presented computations show that more advanced turbulence models are able to describe many of the important features of the diffuser flow but that both more model development and better knowledge of the physics of separating flows are needed to further improve the predictions.

3.3. Separation control model

A new way of modelling the effects of vortex generators in flows where one spatial direction is homogeneous is presented in paper 3. The increased mixing due to the vortex generators is introduced as additional Reynolds stresses through a source term in the Reynolds stress equations. The magnitude of the source term is determined by a model for the vortex generators that is based on wing-theory and the Lamb-Oseen model for viscous vortices. The model takes into account the oncoming flow distribution and use volume forces to account for the induced drag of the vortex generators.

The model was used to test how the position of the vortex generator in the plane asymmetric diffuser affect their efficiency. The integrated flux of

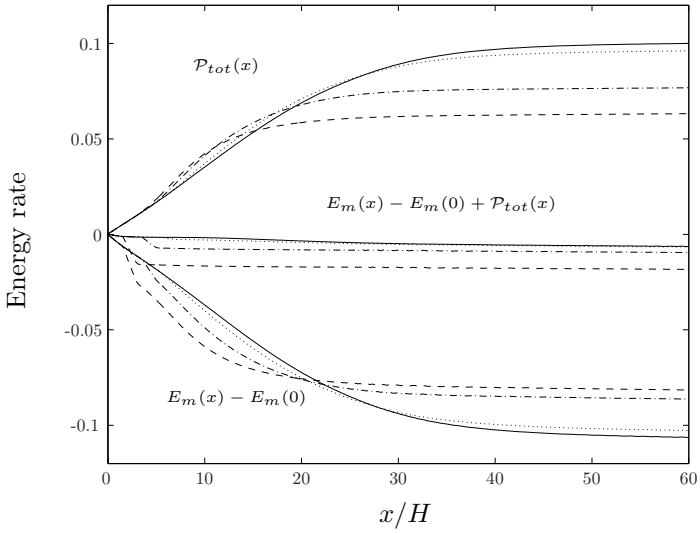

FIGURE 3.6. Redistribution of energy through the diffuser. Line styles corresponds to different x_{VG}-positions of the vortex generators: (——) unperturbed, (− −) $1.3H$, (−·−) $3.3H$, (· · ·) $5.3H$. The lowest set of curves shows the flux of mechanical energy, $E_m(x) - E_m(0)$. The uppermost set of curves shows the total turbulent kinetic energy production, $\mathcal{P}_{tot}(x)$.

mechanical energy over a cross-section,

$$E_m(x) = \int U(x,y) \left(P(x,y) + \frac{1}{2}\rho \left(U(x,y)^2 + V(x,y)^2 \right) + \rho \overline{uu}(x,y) \right) \mathrm{d}y, \tag{3.14}$$

shown in the lower set of curves in figure 3.6, was used as a measure of the total efficiency. The decrease of this quantity is a measure of the total pressure loss and it was found that E_m decreases mainly as a consequence of production of turbulence kinetic energy. This is shown in figure 3.6 where also the integrated production rate of turbulent kinetic energy,

$$\mathcal{P}_{tot}(x) = \int_0^x \int \rho \mathcal{P}(x', y) \mathrm{d}y \mathrm{d}x' \quad \text{where} \quad \mathcal{P} = -\overline{u_i u_j} \frac{\partial U_i}{\partial x_j}, \tag{3.15}$$

is plotted in the uppermost set of curves. The middle set of curves is the sum of E_m and $\mathcal{P}_{tot}$ and can be seen as a representation of the losses due to viscous dissipation and retardation due to the vortex generator drag.

It is apparent from figure 3.6 that in the more efficient configurations the major losses of mechanical energy occur more upstream in the diffuser due to the combined effect of the vortex generator drag and an increase in production rate there. It can also be seen that the increased efficiency is entirely due to

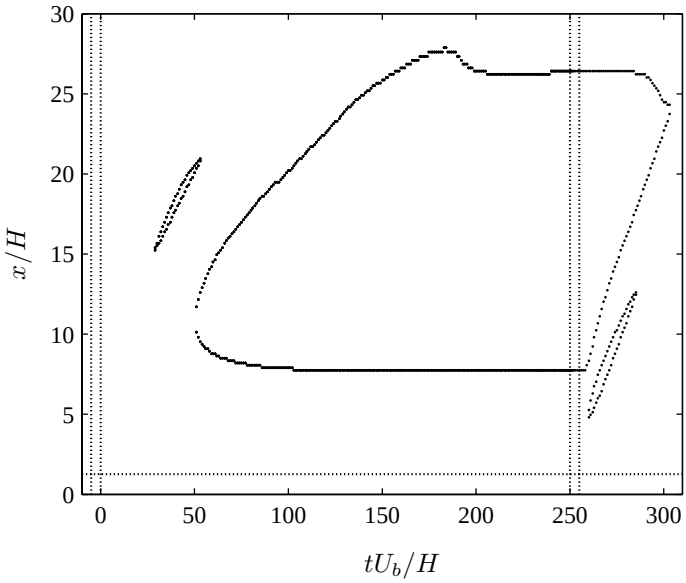

FIGURE 3.7. Separation and reattachment points as functions of time after the forcing is removed and subsequently applied.

a lower integrated production rate of turbulence and that the total pressure losses due to vortex generator drag and viscous dissipation are larger for the more efficient cases.

Profiles of the streamwise velocity reveal that the momentum transfer towards the inclined wall is very efficient in the beginning of the diffuser in the two cases with x_{VG}=1.3 and 3.3. The large levels of momentum near the wall decrease the sensitivity to the adverse pressure gradient and prevent separation. This is achieved by increasing the turbulent momentum diffusion near the wall at an early stage in the diffuser thus avoiding the formation of a separation and a large, strong, turbulence producing shear-layer. The turbulence levels in the worst performing case, x_{VG}=5.3, increase to approximately twice the magnitude of the other cases due to this, which is comparable to the levels in the uncontrolled case. The most efficient of the cases is the one with the flattest velocity profiles and hence with the smallest regions of large mean shear, reflecting the fact that turbulence production, which is proportional to the mean shear, is the major cause of energy losses in this flow.

The temporal evolution of the separation after the vortex generator control is turned off and then on again was investigated using time-accurate quasi-steady RANS-computations. The instantaneous separation and reattachment points are shown in figure 3.7, the dotted vertical line-pairs on the left and right hand sides of the figure indicate the regions where the forcing is ramped down

and up respectively. The vortex generator location, indicated by a horizontal dotted line, and parameters are the same as in the case with x_{VG}=1.3.

We can see that it takes approximately 30 non-dimensional units of time before any separation is formed on the inclined wall, and then it is only a relatively small separation that drifts downstream and eventually disappears. The main separation does not form until 50 time units have passed since the forcing was totally turned off. The main separation spreads out from a position near x/H=11 and reaches a stationary state at $tU_b/H\approx$200 after some transient behaviour where it for a while is larger than the stationary size. The separation point position becomes stationary relatively early as compared to the reattachment point.

When the control subsequently is turned on again the response is surprisingly quick, the separation length starts to diminish 4 units of time after the forcing has reached full strength. A short separated region forms around x/H=5, moves downstream and disappears. The main separation diminishes in a manner, close to, linear with time as the separation point moves downstream. The reattachment point is for nearly 30 units of time unaffected by the control and after approximately 50 time units the separation is totally removed.

An analysis of the instantaneous flow losses during the above described cycle indicates that a net gain could be achieved by turning the control on and off in a cyclic manner.

3.4. Negative production in the reattachment zone

The influences that negative production rates of turbulence kinetic energy may have on the reattachment flow of a separation are discussed in paper 5 of the thesis. A scenario explaining how negative production of turbulent kinetic energy can occur in the reattachment region of separating flows is presented together with data supporting the described scenario.

The production rate of turbulence kinetic energy appears in both the transport equation for the mean-flow kinetic energy and in the transport equation for the turbulent kinetic energy. The production term has opposite sign in the two equations and is normally a dissipative sink term for the mean-flow and consequently normally a source term for the turbulence. Several previous investigations of turbulent separating flows have reported negative production rates, but the magnitude of the negative values have been considered small in comparison with other terms in the turbulence kinetic energy equation. However, in a comparison with the terms in the mean-flow kinetic energy equation, the negative production rates may very well be of significant magnitude. Such a comparison is shown in figure 3.8 and it is easy to see that the negative values plays an important role for the balance of the mean-flow kinetic energy.

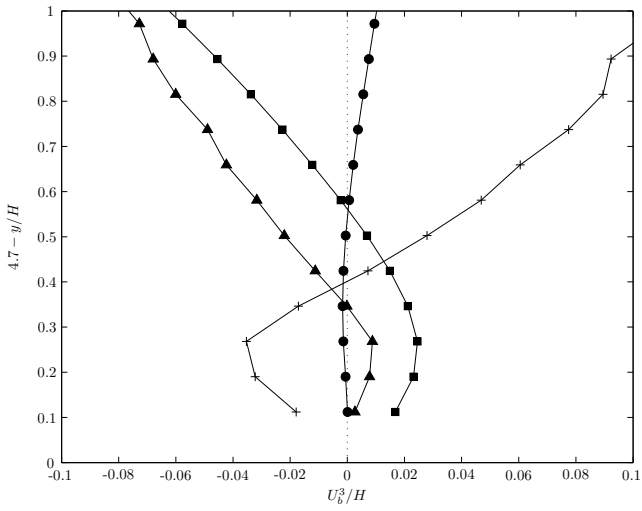

FIGURE 3.8. Measured budget for terms in the transport equation for mean-flow kinetic energy. (▲) production rate of turbulent kinetic energy, (■) transport related to the mean pressure, (•) advective transport, (+) turbulent diffusion.

Negative production can explain the frequently reported rapid decay of the Reynolds stresses in the vicinity of reattachment. The turbulent energy is partly transferred to the mean flow.

It is also possible that negative production can explain why nearly all turbulence models predict a too small magnitude of the reversed flow velocity in separated flows. Transfer of energy from the turbulence to the mean reversed flow can explain what is missing in the models, in order to capture the correct backflow velocity magnitude.

CHAPTER 4

Concluding remarks and outlook

Different aspects of the flow in a plane asymmetric diffuser with an 8.5° opening angle have been investigated in the present thesis. A majority of the conclusions drawn are believed to be applicable and of importance also in other separating flows.

The experimental investigation of the mean flow and turbulence properties revealed a flow with several interesting characteristics: strong and suddenly imposed shearing, non-equilibrium turbulence, separation, reattachment and turbulence relaxation. All these flow-features are important for turbulence models to predict in an accurate manner in order to get reasonably accurate solutions of the flow as a whole. Evaluation of stereoscopic PIV-data either requires large computational resources or lots of time, therefore there are still many features of the flow that could be investigated, using the already collected images.

The investigation of flow structures revealed some new interesting features of the separating flow. Most interesting is perhaps the inclined structures of the spanwise velocity fluctuations, clearly seen both in the instantaneous realisations of the flow and in the two-point correlations. I have not been able to find any previous report mentioning these kinds of structures, the reasons for this is probably that stereoscopic PIV measurements are still quite rare. The structures can be seen in for example figure 21 in Le *et al.* (1997), showing an instantaneous field, but the structures are not commented in the text. The role of these structures for the flow is still unclear, but observations made in this thesis indicate that they are likely to be signatures of 'hair-pin like' structures. Further investigations of these structures is one natural continuation of the present work.

The two papers involving turbulence modelling indicate that accurate predictions of the diffuser flow are within reach of today's more advanced turbulence models, but that both models tested had problems with predicting correctly the back flow rate and the long range momentum diffusion occurring after reattachment.

Connected to turbulence modelling is also the finding in paper 5, that negative production rates of turbulent kinetic energy are of importance for the back-flow region. Although DRSMs theoretically can reproduce negative

production they are usually not formulated with this phenomenon in focus. Therefore an investigation of model requirements for correct correct predictions of negative production rates is needed. With the EARSM formulation used in Wallin & Johansson (2000) it is not possible to predict negative production.

The vortex generator model is perhaps the result of this thesis that most directly could be useful in engineering fluid mechanics. Some interesting results were also found when applying the model to the diffuser flow. A maybe not so surprising but still important observation was that a vast majority of the flow losses in the diffuser can be directly related to the production of turbulence. The time accurate computations of the formation and removal of a separation give good hope of being able to increase the energy efficiency of the control by successively turning it on and off. This type of quasi-steady results are produced naturally in the present implementation since the system of equations is iterated to steady state in a time-accurate manner. This is however in many cases unnecessarily time consuming, and a continuation of the work on the vortex generator model should include developing a faster route to the steady state solution of the system of RANS and DRSM equations. Then, if the computations are reasonably fast, optimisation of the vortex generator parameters could be performed.

Acknowledgements

First of all, I would like to express my gratitude to my supervisor Professor Arne Johansson for accepting me as his student and for sharing with me parts of his great knowledge in turbulence. I especially appreciate how he has always taken time to discuss my work, seemingly independent of his own workload.

I would also like to thank my co-worker, friend and former office-mate Björn Lindgren for introducing me to the field of fluid mechanics experiments and for being an excellent collaborator.

Special thanks to Stefan Wallin, for his experienced guidance in turbulence modelling and computations as well as for reading and commenting the manuscript of my thesis. Many thanks also to Timmy Sigfrids and Svante Törnblom for their valuable comments on the manuscript.

Gustav Amberg and Minh Do-Quang are acknowledged for answering numerous questions related to the FEMLego package.

I am very grateful to everyone at the department of mechanics for contributing to a stimulating, enjoyable, friendly and relaxed atmosphere. I have particularly enjoyed the coffee breaks, not so much for the coffee as for the vivid discussions and many laughs.

The Swedish Energy Agency are gratefully acknowledged for financing my doctoral studies. The PIV measurement system was acquired with funding from the Knut and Alice Wallenberg foundation which is also gratefully acknowledged.

Lastly and most importantly, I want to thank my wife Jenny and my son Kalle, for their love.

Bibliography

Adrian, R. J., Meinhart, C. D. & Tomkins, C. D. 2000 Vortex organization in the outer region of the turbulent boundary layer. *J. Fluid Mech.* **422**, 1–54.

Alving, A. & Fernholz, H. 1995 Mean velocity scaling in and around a mild, turbulent separation bubble. *Phys. Fluids* **7**, 1956–1969.

Alving, A. & Fernholz, H. 1996 Turbulence measurements around a mild separation bubble and downstream of reattachment. *J. Fluid Mech.* **322**, 297–328.

Angele, K. 2003 Experimental studiens of turbulent boundary layer separation and control. Ph.D. Thesis, Department of Mechanics, KTH, Stockholm, Sweden, TRITA-MEK 2003:08.

Angele, K. P. & Muhammad-Klingmann, B. 2005 PIV measurements in a weakly separating and reattaching turbulent boundary layer. *Eur. J. Mech. B/Fluids* **25**, 204–222.

Apsley, D. D. & Leschziner, M. A. 1999 Advanced turbulence modelling of separated flow in a diffuser. *Flow, Turbulence and Combustion* **63**, 81—112.

Armaly, B. F., Durst, F., Pereira, J. C. F. & Schönung, B. 1983 Experimental and theoretical investigation of backward-facing step flow. *J. Fluid Mech.* **127**, 473–496.

Bradbury, L. J. S. & Castro, I. P. 1971 A pulsed-wire technique for velocity measurements in highly turbulent flows. *J. Fluid Mech.* **49**, 657–691.

Bradshaw, P. & Wong, F. Y. F. 1972 The reattachment and relaxation of a turbulent shear layer. *J. Fluid Mech.* **52**, 113–135.

Brunet, L., Calzalbou, J. B., Chassaing, P. & Jervase, L. 1997 Experimental and computational study of pressure effects on turbulent flow in an asymmetric plane diffuser. In *11th Symp. on Turbulent Shear Flows, Grenoble, France*, pp. 114–119.

Buice, C. U. & Eaton, J. K. 1997 Experimental investigation of flow through an asymmetric plane diffuser. *Tech. Rep.*. Department of mechanical engineering, Stanford university.

Buice, C. U. & Eaton, J. K. 2000 Experimental investigation of flow through an asymmetric plane diffuser. *J. Fluids Eng.* **122**, 433–435.

Carlier, J. & Stanislas, M. 2005 Experimental study of eddy structures in a

turbulent boundary layer using particle image velocimetry. *J. Fluid Mech.* **535**, 143–188.

Castro, I. P. & Haque, A. 1987 The structure of a shear layer bounding a separation region. *J. Fluid Mech.* **179**, 439–468.

Cherry, N. J., Hillier, R. & Latour, M. E. M. P. 1984 Unsteady measurements in a separated and reattaching flow. *J. Fluid Mech.* **144**, 13–46.

Chou, P. Y. 1945 On velocity correlations and the solutions of the equations of turbulent motion. *Brown University – Quart. App. Math.* **3** (1), 38–54.

Dengel, P. & Fernholz, H. 1990 An experimental investigation of an incompressible turbulent boundary layer in the vicinity of separation. *J. Fluid Mech.* **212**, 615–636.

Dianat, M. & Castro, I. P. 1991 Turbulence in a separated boundary layer. *J. Fluid Mech.* **226**, 91–123.

Etheridge, D. W. & Kemp, P. H. 1978 Measurements of turbulent flow downstream of a rearward-facing step. *J. Fluid Mech.* **86**, 545–566.

Gullman-Strand, J. 2004 Turbulence and scalar flux modelling applied to separated flows. PhD. Thesis, KTH Mechanics, Stockholm, Sweden, TRITA-MEK 2004:16.

Hancock, P. E. 1999 Measurements of mean and fluctuating wall shear stress beneath spanwise-invariant separation bubbles. *Exp. in Fluids* **27**, 53–59.

Hancock, P. E. 2000 Low reynolds number two-dimensional separated and reattaching turbulent shear flow. *J. Fluid Mech.* **410**, 101–122.

Head, M. & Bandyopadhyay, P. 1981 New aspects of turbulent boundary-layer structure. *J. Fluid Mech.* **107**, 297–338.

Hellsten, A. & Rautaheimo, P., ed. 1999 *Workshop on refined turbulence modelling*. ERCOFTAC/IAHR/COST.

Herbst, A. H., Schlatter, P. & Henningson, D. S. 2006 Simulations of turbulent flow in a plane asymmetric diffuser. *To be published* .

Jovic, S. & Driver, D. 1994 Backward-facing step measurements at low Reynolds number, Re_h=5000. NASA technical memorandum 108807. Ames research center.

Jovic, S. & Driver, D. 1995 Reynolds number effect on the skin friction in separated flows behind a backward-facing step. *Exp. in Fluids* **18** (6), 464–467.

Kaltenbach, H.-J., Fatica, M., Mittal, R., Lund, T. S. & Moin, P. 1999 Study of flow in a planar asymmetric diffuser using large-eddy simulation. *J. Fluid Mech.* **390**, 151–185.

Kasagi, N. & Matsunaga, A. 1995 Three-dimensional particle-tracking velocimetry measurements of turbulence statistics and energy budget in a backward-facing step flow. *Int. J. Heat and Fluid flow* **16**, 477–485.

Kiya, M. & Sasaki, K. 1983 Structure of a turbulent separation bubble. *J. Fluid Mech.* **137**, 83–113.

Kiya, M. & Sasaki, K. 1985 Structure of large-scale vortices and unsteady reverse flow in the reattaching zone of a turbulent separation bubble. *J. Fluid Mech.* **154**, 463–491.

Kolmogorov, A. N. 1942 Equations of turbulent flow of an incompressible viscous liquid. *Journal of Physics – USSR* **6** (5), 227–228.

Launder, B., Reece, G. & Rodi, W. 1975 Progress in the development of a Reynolds-stress turbulence closure. *J. Fluid Mech.* **68**, 537–566.

Le, H., Moin, P. & Kim, J. 1997 Direct numerical simulation of turbulent flow over a backward-facing step. *J. Fluid Mech.* **330**, 349–374.

Manceau, R. 2005 An improved version of the elliptic blending model application to non-rotating and rotating channel flows. In *Turbulence and shear flow phenomena 4*.

Moin, P. & Kim, J. 1997 Tackling turbulence with supercomputers. *Scientific American Magazine* .

Na, Y. & Moin, P. 1998 Direct numercial simulation of a separated turbulent boundary layer. *J. Fluid Mech.* **374**, 379–405.

Obi, S., Aoki, K. & Masuda, S. 1993*a* Experimental and computational study of turbulent separating flow in an asymmetric plane diffuser. In *Ninth Symp. on Turbulent Shear Flows*, p. 305. Kyoto, Japan.

Obi, S., Ishibashi, N. & Masuda, S. 1997 The mechanism of momentum transfer enhancement in periodically perturbed turbulent separated flow. In *2nd Int. Symp. on Turbulence, Heat and Mass Transfer, Delft, The Netherlands*, pp. 835–844.

Obi, S., Nikaido, H. & Masuda, S. 1999 Reynold number effect on the turbulent separating flow in an asymmetric plane diffuser. In *Proceedings of FEDSM99*, *FEDSM* 99-6976. ASME/JSME Fluids Engineering Division Summer Meeting.

Obi, S., Ohizumi, K., Aoki, K. & Masuda, S. 1993*b* Turbulent separation control in a plane asymmetric diffuser by periodic perturbation. In *Engineering turbulence modelling and Experiments 2*, pp. 633–642.

Perry, A. E. & Fairlie, B. D. 1975 A study of turbulent boundary-layer separation and reattachment. *J. Fluid Mech.* **69**, 657–672.

Raffel, M., Willert, C. & Kompenhans, J. 1997 *Particle Image Velocimetry, A practical guide*. Springer Verlag.

Robinson, S. 1991 Coherent motions in the turbulent boundary layer. *Ann. Rev. Fluid Mech.* **23**, 601–639.

Rott, N. 1990 Note on the history of the Reynolds number. *Ann. Rev. Fluid Mech.* **22**, 1–11.

Ruderich, R. & Fernholz, H. H. 1975 An experimental investigation of a turbulent shear flow with separation, reverse flow, and reattachment. *J. Fluid Mech.* **163**, 283–322.

Scarano, F., David, L., Bsibsi, M. & Calluaud, D. 2005 S-PIV comparative assessment: image dewarping+misalignment correction and pinhole+geometric back projection. *Exp. in Fluids* **39**, 257–266.

Shiloh, B. G., Shivaprasad, B. G. & Simpson, R. L. 1981 The structure of a separating turbulent boundary layer. Part 3. Transverse velocity measurements. *J. Fluid Mech.* **113**, 75–90.

Sigurdson, L. 1995 The structure and control of a turbulent reattaching flow. *J. Fluid Mech.* **298**, 139–165.

Simpson, R. L. 1989 Turbulent boundary-layer separation. *Ann. Rev. Fluid Mech.* **21**, 205–234.

Simpson, R. L., Chew, Y.-T. & Shivaprasad, B. G. 1981*a* The structure of a separating turbulent boundary layer. Part 1. Mean flow and Reynolds stresses. *J. Fluid Mech.* **113**, 23–51.

Simpson, R. L., Chew, Y.-T. & Shivaprasad, B. G. 1981*b* The structure of a separating turbulent boundary layer. Part 2. Higher order turbulence results. *J. Fluid Mech.* **113**, 53–73.

Sjögren, T. & Johansson, A. V. 2000 Development and calibration of algebraic nonlinear models for terms in the Reynolds stress transport equations. *Phys. Fluids* **12** (6), 1554–1572.

Skote, M. & Henningson, D. 2002 Direct numercial simulation of a separated turbulent boundary layer. *J. Fluid Mech.* **471**, 107–136.

Song, S., DeGraaff, D. B. & Eaton, J. K. 2000 Experimental study of a separating, reattaching, and redeveloping flow over a smoothly contoured ramp. *Int. J. Heat and Fluid flow* **21**, 512–519.

Song, S. & Eaton, J. K. 2002*a* The effects of wall roughness on the separated flow over a smoothly contoured ramp. *Exp. in Fluids* **33**, 38–46.

Song, S. & Eaton, J. K. 2002*b* Reynolds number effects on a turbulent boundary layer with separation, reattachment, and recovery. Technical report TSD-146. Mechanical engineering department, Stanford university.

Song, S. & Eaton, J. K. 2004*a* Flow structures of a separating, reattaching and recovering boundary layer for a large range of Reynolds number. *Exp. Fluids* **36**, 642–653.

Song, S. & Eaton, J. K. 2004*b* Reynolds number effects on a turbulent boundary layer with separation, reattachment, and recovery. *Exp. in Fluids* **36**, 246–258.

Spalart, P. R. & Coleman, G. N. 1997 Numerical study of a separation bubble with heat transfer. *Eur. J. Mech. B/Fluids* **16** (2), 169–189.

Speziale, C. G., Sarkar, S. & Gatski, T. B. 1991 Modelling the pressure-strain correlation of turbulence: an invariant dynamical systems approach. *J. Fluid Mech.* **227**, 245–272.

Stanislas, M., Okamoto, K., J., K. C. & Westerweel, J. 2005 Main results of the second international PIV challenge. *Exp. in Fluids* **39**, 170–191.

Stratford, B. S. 1959 An experimental flow with zero skin friction troughout its region of pressure rise. *J. Fluid Mech.* **5**, 17–35.

Sveningsson, A. 2006 Turbulence transport modelling in gas turbine related applications. PhD thesis, Chalmers Tekniska Högskola.

Tropea, C. 1995 Laser Doppler anemometry: recent developments and future challenges. *Meas. Sci. Technol.* **6**, 605–619.

Wallin, S. & Johansson, A. V. 2000 An explicit algebraic Reynolds stress model for incompressible and compressible turbulent flows. *J. Fluid Mech.* **403**, 89–132.

Wallin, S. & Johansson, A. V. 2002 Modelling streamline curvature effects in explicit algebraic Reynolds stress turbulence models. *Int. J. Heat and Fluid Flow* **23**, 721 – 730.

Westerweel, J. 1993 Digital particle image velocimetry - theory and application. PhD thesis, Technische Universiteit Delft.

Wieneke, B. 2005 Stereo-PIV using self-calibration on particle images. *Exp. in Fluids* **39**, 267–280.

Wilcox, D. C. 1988 Reassessment of the scale-determining equation for advanced turbulence models. *AIAA Journal* **26** (11), 1299–1310.

Wilcox, D. C. 1994 Simulation of transition with a two-equation turbulence model. *AIAA Journal* **32** (2), 247–255.

Wu, X., Schlüter, J., Moin, P., Pitsch, H., Iaccarino, G. & Ham, F. 2006 Computational study on the internal layer in a diffuser. *J. Fluid Mech.* **550**, 391–412.

Yin, J.-F. & Yu, S.-Z. 1993 Investigation of turbulent separation-reattachment flow in a curved-wall diffuser. *Int. J. Heat and Fluid flow* **14** (2), 129–137.

Yoshioka, S., Obi, S. & Masuda, S. 2001*a* Organized vortex motion in periodically perturbed turbulent separated flow over a backward-facing step. *Int. J. Heat and Fluid flow* **22**, 301–307.

Yoshioka, S., Obi, S. & Masuda, S. 2001*b* Turbulence statistics of periodically perturbed separated flow over backward facing step. *Int. J. Heat Fluid Flow* **22**, 391–401.

Paper 6

P6

Experimental procedures for the investigation of the turbulent flow in a plane asymmetric diffuser by means of stereoscopic high-speed PIV

By Olle Törnblom, Björn Lindgren and Arne V. Johansson

KTH Mechanics, SE-100 44 Stockholm, Sweden

Technical report

The design process of an experimental setup for studying a plane asymmetric diffuser flow is described. Prior to the diffuser the flow passes through a 3 m long and 30 mm high channel to generate a turbulent channel flow as inlet condition to the diffuser. The wind-tunnel is of closed circuit type in order to allow for flow seeding in an indoor environment. The wind-tunnel is driven by an 11 kW radial fan, capable of generating inlet channel flow Reynolds numbers of up to HU_{cl}/ν =60000, H being the channel height and U_{cl} the channel centreline velocity. The setup and calibration of a stereoscopic high-speed PIV-system is described in detail and the measurement circumstances important for the quality of the PIV-data are scrutinised.

1. Introduction

Study of diffuser flows, *i.e.* duct flows subjected to an adverse pressure gradient, is motivated by the large number of applications in which these flows appear and the energy savings that may result from an increased knowledge about proper diffuser designs and separation control. The experimental facility whose design is described herein was built to study a generic flow with separation, both in order to get a database for turbulence model comparisons as well as to study the fundamental physics of the flow.

If one desires to study turbulent separating flow, separation control and provide reference data for computations, in the same geometry, it has to be chosen with care. The most generic way to study separation is to do a flat plate experiment where an adverse pressure gradient is produced by altering the free-stream velocity with a variable geometry of the opposing wind-tunnel wall (see *e.g.* Perry & Fairlie (1975) and Angele & Muhammad-Klingmann (2005)). Dianat & Castro (1991) used a porous cylinder with a small flap at the trailing edge mounted above a flat plate to generate the pressure gradient.

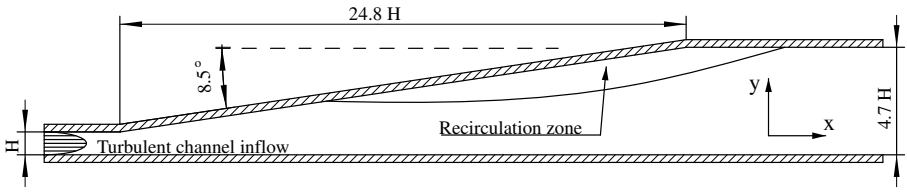

FIGURE 1. The plane asymmetric diffuser.

Another category of separated flows is that associated with sharp edges or bluff body geometries. Examples are flow over flat plates or cylinders with blunt leading edges (*e.g.* Cherry *et al.* (1984) and Ruderich & Fernholz (1975)) or flow over a backward facing step (*e.g.* Etheridge & Kemp (1978) and Yoshioka *et al.* (2001)). Symmetric diffuser flows have been investigated by *e.g.* Sovran & Klomp (1967) and Chithambaran *et al.* (1984). All of these flow cases have been used to study different aspects of separation, but some are more suited for the study of generic mechanisms and comparison between experiments and numerical simulations. In blunt edge flows and flows over backward facing steps the challenge of predicting the separation point vanishes, as the separation inevitably will occur at the corner. In symmetric diffusers the separation can fluctuate between the two diffuser walls in a random manner and at long time-scales making ensemble averaging a very tedious task. In a CFD calculation, this unstable flow situation may also cause convergence problems.

The plane asymmetric diffuser with turbulent channel inflow, shown in figure 1, has the properties we were looking for. The fully developed turbulent channel flow used as inflow condition is a well known flow, simplifying the task of setting appropriate boundary conditions, both in turbulence model computations and in direct numerical simulations. The asymmetric geometry favours separation on the inclined wall and eliminates the problems associated with symmetric diffusers. If the upstream corner of the inclined wall is sufficiently smooth with a finite radius of curvature, the separation point will be located at the inclined wall, giving a challenging flow to predict in simulations and a location of the separation point sensitive to control. Furthermore, the relatively simple geometry with two dimensional flow and mostly straight walls facilitate CFD grid generation and the determination of positions inside the measurement section.

2. Design

2.1. *Pre-design considerations*

At the time when the first design steps were taken, there existed two (to the authors known) previous experiments in a very similar geometry *i.e.* those by Obi

et al. (1993) and Buice & Eaton (1997). In particular the latter one, which contains a detailed description of the experimental setup, was studied in order to learn about the difficulties related to the design of a plane asymmetric diffuser experiment. The major difficulty of this flow case is the inherent tendency, of a separating flow, to be three-dimensional. Since we required the flow to be two-dimensional (in an average sense), the three-dimensional behaviour must be controlled. The undesired three-dimensional effects enter the flow via the end walls (the walls which limit the spanwise extent of the diffuser), hence an ideal, but unrealistic, solution would be to have an infinitely wide diffuser. However, a relatively large spanwise width compared to the height of the diffuser (*i.e.* a large aspect ratio) is a necessary requirement to have a two-dimensional flow field.

A preliminary idea was that the newly built low speed wind-tunnel at the department (*cf.* Lindgren & Johansson (2002)) could be used for the experiment. But that alternative was abandoned due to the large pressure losses that the inlet channel would cause and because of the limited aspect ratio it would allow.

Another decision which needs to be taken before the actual design-work start is how large the diffuser should be. The size of the facility partly determines what Reynolds number the flow will have and also what fan power is needed to drive the wind-tunnel at the desired flow speeds. In a small facility the flow will be more influenced by small imperfections in the design *e.g.* small edges in joints between different wall sections. A too small test-section also limits the accessibility, due to the physical size of our hands, arms etc. and it also requires better precision in the positioning of the measurement probe than in a larger test-section, for the same relative error.

With these arguments in mind we decided to make our diffuser larger than the ones used in the experiments by Obi *et al.* (1993) and Buice & Eaton (1997). We also wanted a larger aspect ratio than the previous experiments. Obi's and Buice's inlet channel heights were 20 mm and 15 mm and their spanwise widths were 700 mm and 450 mm respectively. We chose to build a 30 mm high channel and an inlet aspect ratio of 50, giving a channel width of 1500 mm (due to the standard width of plywood sheets the final channel was built with a width of 1525 mm). In turbulent channel flow an aspect ratio of five is the lowest possible in order to have (a reasonably) two-dimensional flow in an about two channel heights wide region in the centre of the channel (Johansson & Alfredsson (1986)). If the aspect ratio is lower than this, secondary flow effects caused by end walls and corners may influence the flow. In our facility this requirement is well fulfilled also in the exit channel where the aspect ratio is 10.8. However, in flows with adverse pressure gradients these rules of thumb can only be considered valid if separation is avoided on the end walls.

In order to produce a fully developed turbulent channel flow it was decided that the length of the inlet channel should be at least 100 channel heights. According to the experiments by Comte-Bellot (1965) the higher order statistical moments are fully developed at 60 channel heights from the inlet. Similar observations were made by Johansson & Alfredsson (1982).

Accordingly, the final choice of channel geometry was a 30 mm high, 3000 mm long and 1500 mm wide channel. It was concluded that, in order to minimize the floor area occupied by the wind-tunnel, the channel should be built so that the spanwise direction was oriented vertically, which is also favourable in the sense of minimizing wall deflections caused by gravity.

One of the obvious difficulties when studying separating flows experimentally is the occurrence of velocities with changing sign, due to the region of backflow. This difficulty makes it impossible to measure with hot-wire anemometry, an otherwise well established and accurate technique. If one wants to determine both the value of the velocity and its direction one has a few alternatives; pulsed hot-wires, laser Doppler velocimetry (LDV) or particle image velocimetry (PIV). The natural choice for us was to use the two latter techniques with emphasis on PIV. LDV and PIV are both optical methods, and thereby require optical access to the flow. Hence, the measurement section of the wind-tunnel has to be made in a transparent material. If one wants to make a large transparent wall, as in a wind-tunnel test section, at a reasonable cost one has practically two choices, window glass or polymer glass. Window glass typically has a more even and precise thickness than polymer glass. An even thickness is of high importance when measuring with LDV, since a distortion of the laser-beams (or rather of one of the beams) can make them misaligned in the measurement volume, resulting in bad, or no, Doppler signals. Furthermore, window glass has a higher modulus of elasticity as compared to polymer glass which allows thinner sheets to be used for a certain desired stiffness. Thinner sheets will also contribute to lowering the optical distortion. If one desires to use polymer glass a popular choice is Plexiglas® which is made from polymethyl methacrylate (PMMA). This material is usually cheaper than window glass and not as brittle, furthermore it is easier to machine than window glass. Another material property that could influence the choice is the refractive index, but for PMMA and window glass this can be disregarded since it is approximately 1.5 for both materials. The need to be able to drill pressure taps, the cheaper prize and the possibility to join Plexiglas® sheets together with screws made us choose this material for large parts of the measurement section.

2.2. *Fan and motor*

Having decided the spanwise width and height of the inlet channel and the desired Re_τ in the inlet channel the required flow rate can be calculated using

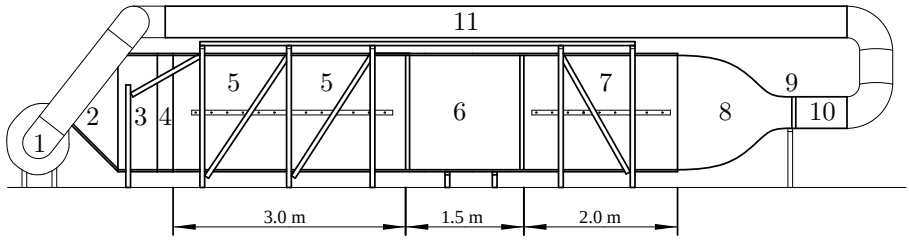

FIGURE 2. A sketch of the complete wind-tunnel. Refer to table 1 for a description of the numbered parts.

Part	Description
1	Fan, 11 kW centrifugal
2	Transformer from 322×229 mm^2 to 1525×100 mm^2
3	Settling chamber, 1525×100×500 mm^3
4	Contraction, from 1525×100 mm^2 to 1525×30 mm^2
5	Inlet channel, 1525×30×3000 mm^3
6	Diffuser/measurement section, from 1525×30 mm^2 to 1525×141 mm^2
7	Exit channel, 1525×141×2000 mm^3
8	Contraction, from 1525×141 mm^2 to 400×300 mm^2
9	Heat exchanger
10	Transformer, from 400×300 mm^2 to 400 mm diameter
11	Return pipe, 400 mm diameter with five 90° bends

TABLE 1. Description of the numbered parts in figure 2.

the logarithmic friction law and Dean's relation,

$$\frac{U_{cl}}{u_\tau} = \frac{1}{\varkappa} \ln\left(\frac{u_\tau H}{2\nu}\right) + C \tag{1}$$

$$\frac{U_{cl}}{U_b} = 1.28 \left(\frac{U_b H}{2\nu}\right)^{-0.0116} \tag{2}$$

with the additive constant $C = 6.0$ and $\varkappa = 0.4$. Where U_{cl} is the channel centreline velocity, u_τ the friction velocity at the wall, U_b the channel bulk velocity and H is the channel height. A desired $Re_\tau = u_\tau H/\nu = 4000$ gives, according to these relations and the chosen channel area, a volume flux of approximately 1.8 m^3/s. In order to choose a fan one has to know also at what pressure the required flow should be delivered. This has to be estimated. A very rough estimate yielded that the wind-tunnel would cause pressure losses corresponding to approximately three times the dynamic pressure of the inlet channel bulk velocity. Later this estimate was proven to be reasonably accurate for the first design, which did not have a return circuit and heat exchanger. When choosing

a fan it is advisable to examine not only the maximum performance, but also the performance over a region of the fan characteristics curve. It is desirable to have a characteristics curve in the volume flow region where the fan will be used, that gives as small a flux variation as possible for a given variation in the pressure, for instance due to a nonstationary separation bubble.

Based on these estimates a centrifugal fan capable of delivering 2.1 m^3/s at 3000 Pa was ordered from Ventur tekniska AB. To control the speed of the 11 kW induction motor, the fan was complemented with a frequency converter and a filter, from ABB Motors AB.

2.3. *Transformer and settling chamber upstream the channel*

The fan has an outlet section of 322×229 mm^2 that has to be transformed into the large aspect ratio cross-section (1525×30 mm^2) of the inlet channel. This transformation had to take place over a limited length, putting high demand on the design in order to minimize losses and ensure an even flow over the whole cross-section.

A common way to achieve a spanwise homogeneous flow is to have a settling or stagnation chamber, with large cross-section area where the velocity is very low, followed by a contraction into the channel. Here, we chose to have a rather small settling chamber with a cross-section area of 1525×100 mm^2. By doing so, the transformer between the fan and the settling chamber will have a shape which diverges in the spanwise direction and contracts in the other direction, see figure 3. The total expansion ratio, *i.e.* the ratio between the cross-section area of the settling chamber and the fan outlet area, is thus only about two. Two splitter plates are mounted immediately after the fan outlet to avoid large scale flow separation here and to direct the flow outwards in the spanwise direction.

Three screens, shown in figure 3, were placed in the transformer and settling chamber in order to even out mean flow variations. The screens used have a wire diameter d of 0.71 mm and a (wire centre to wire centre) mesh width M of 3.2 mm. These values give a porosity $\beta = (1 - d/M)^2 = 0.6$. Using screens will not only even out mean flow variations but also reduce angle deviations relative to the screen according to the relation

$$\phi = \alpha\theta, \tag{3}$$

where θ is the angle of the incoming flow and ϕ the angle of the out-going flow. The constant α is related to the local pressure-loss coefficient K_0 through the empirical relation (see Laws & Livesey (1978))

$$\alpha = \frac{1.1}{\sqrt{1 + K_0}}. \tag{4}$$

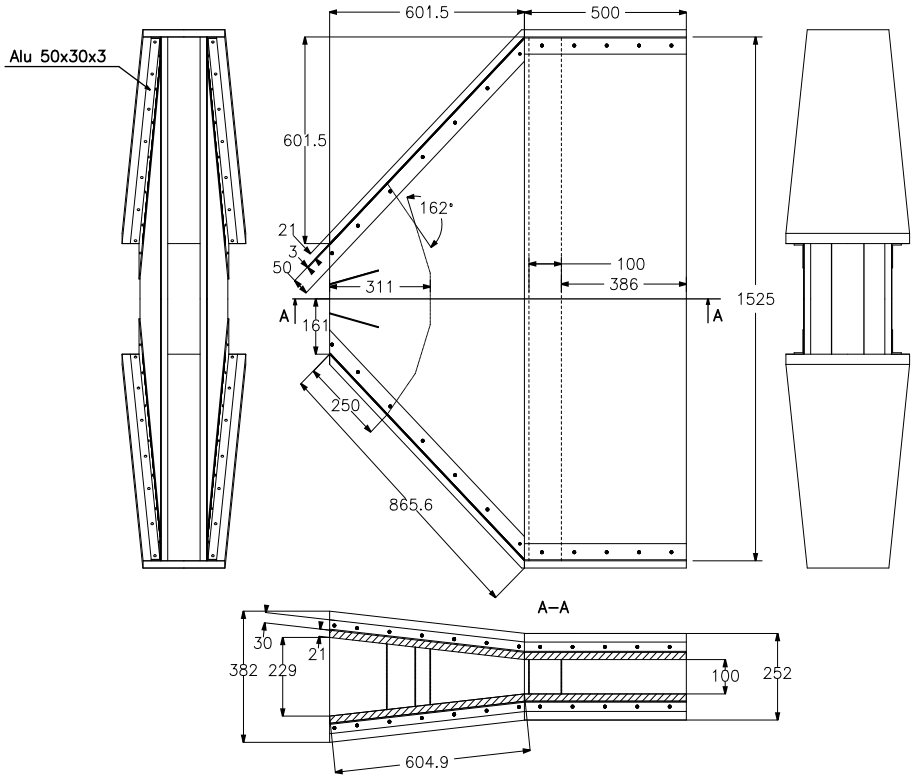

FIGURE 3. Four view drawing of the transformer and settling chamber upstream the channel.

The local pressure-loss coefficient is highly Reynolds number dependent for subcritical Reynolds numbers but can for higher Reynolds numbers be approximated with

$$K_0 = 0.5\frac{1-\beta^2}{\beta^2}, \tag{5}$$

if $0.6 < \beta < 0.7$. With a volume flow of 2.1 m^3/s the wire-diameter Reynolds number will be well above the critical value of $Re_d = 100$. Using equations 4 and 5 it can be seen that the local pressure-loss coefficient will be $K_0 = 0.9$ and that an error in the incoming flow angle relative to the screen will be reduced by a factor 0.8 after the screen. Streamwise mean velocity variations are reduced when the flow passes through a screen according to the expression

$$\frac{\Delta u_2}{\Delta u_1} = \frac{1+\alpha-\alpha K_0}{1+\alpha+K_0}, \tag{6}$$

derived by Taylor & Batchelor (1949), where Δu_1 and Δu_2 are the variations of the streamwise mean velocity upstream and downstream the screen respectively. For the screens of concern herein this ratio will be 0.4.

In the diffusing part, a bent screen was used in order to both even out mean velocity variations and to direct the flow according to equation 3. Further downstream, in the first part of the settling chamber, two screens are placed to further reduce possible mean flow variations. The screens were mounted onto frames made from 15×15 mm stainless steel tubes and were manufactured by AB Derma in Gråbo, Sweden.

Both the transformer and the settling chamber were manufactured in plywood sheets joined together with L-shaped aluminium profiles and screws and sealed with tightening material. All the wind-tunnel parts are mounted in a framework (as can be seen in figure 2) of 60×40×3 mm^3 and 60×40×4 mm^3 steel tubes and steel L-profiles respectively. The steel framework is bolted to the concrete floor in the laboratory.

2.4. *Contraction and inlet channel*

The settling chamber is followed by a two-dimensional contraction, changing the channel height from 100 mm to 30 mm. The shape of the contraction, shown in figure 4, is described by two sinus hyperbolic functions according to the description in Lindgren & Johansson (2002). This shape is an optimal shape regarding the pressure gradient along the walls and it was derived originally for the MTL wind-tunnel by Henrik Alfredsson and Alexander Sahlin at the department, using inviscid/boundary layer calculations. The contraction was manufactured in polystyrene foam that was cut to the appropriate shape using a hot-wire saw. The polystyrene foam was covered with a glassfiber-epoxy laminate in order to have a smooth and hard surface.

The inlet channel consists of two 3000×1525×21 mm^3 plywood sheets with plywood end walls joined together with L-shaped aluminium profiles. Four L-shaped aluminium profiles oriented in the spanwise direction are screwed to the large plywood sheets in order to prevent the walls from bulging due to the larger pressure inside the channel. Furthermore, the large plywood sheets are supported along their centrelines with adjustable screws in order to ensure a constant (30 mm) channel height at all locations. The channel height was measured with a movable 30 mm plastic cube (mounted on a long stick to be able to reach all points in the channel) and adjusted with the screws. The horizontal bar with the adjustment screws can be seen in figure 2.

2.5. *Measurement section*

The measurement section (part number 6 in figure 2) is connected to the inlet channel and the exit channel with high precision joints milled in aluminium with steel guide taps. The joints are held together with three DE-STA-CO®

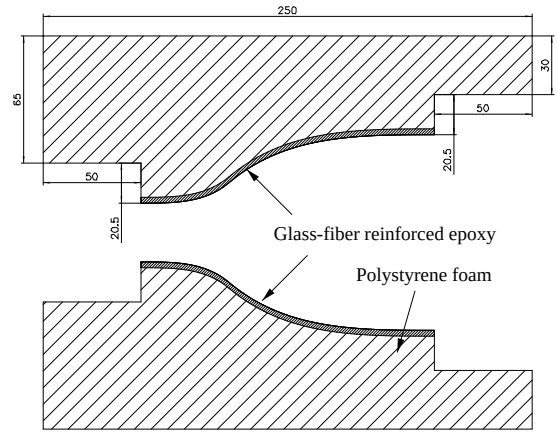

FIGURE 4. The design for the contraction before the inlet channel

clasps at each side. This design allows the measurement section to be removed in order to facilitate modification of the diffuser or measurement installations.

As mentioned in section 2.1, optical access to the measurement section is necessary and Plexiglas® was believed to be the most appropriate transparent material. The plane wall of the measurement section was made from a single $1500\times1525\times25$ mm^3 Plexiglas® sheet and the end walls are two $350\times1500\times25$ mm^3 sheets. It was discovered that the delivered Plexiglas® varied in thickness as much as ±1 mm, and later on a 4 mm thick float-glass window was inserted to replace the Plexiglas® in the upper end wall. The 1250×155 mm^2 piece of float-glass was taken from the mid portion of a large glass plate where the thickness homogeneity are best according to a representative for Pilkington floatglas AB in Halmstad, Sweden. The plane wall and the end walls are joined with screws that go through the end walls and are screwed into threaded holes in the plane wall.

The wall opposite to the straight, *i.e.* the wall that is partly inclined, is built up by several different parts and materials. The photograph in figure 5 shows the structure of this wall. The inlet channel part of this wall is made from 25 mm plexiglas, this section which is approximately 200 mm long is screwed to the flange of the upstream corner. The upstream and downstream corners, depicted in figure 6, are made of solid aluminium that was CNC machined to get well defined radii of curvature, the flanges with threaded holes ensure good alignment between the corner parts and the connected wall sections. Three horizontal aluminium beams extend between the two vertical corner beams (see figure 5), a 4 mm thick glass window is held between the upper and the middle beam. The window gives optical access to the measurement section from two directions and reduces wall reflections, allowing for measurements closer to the

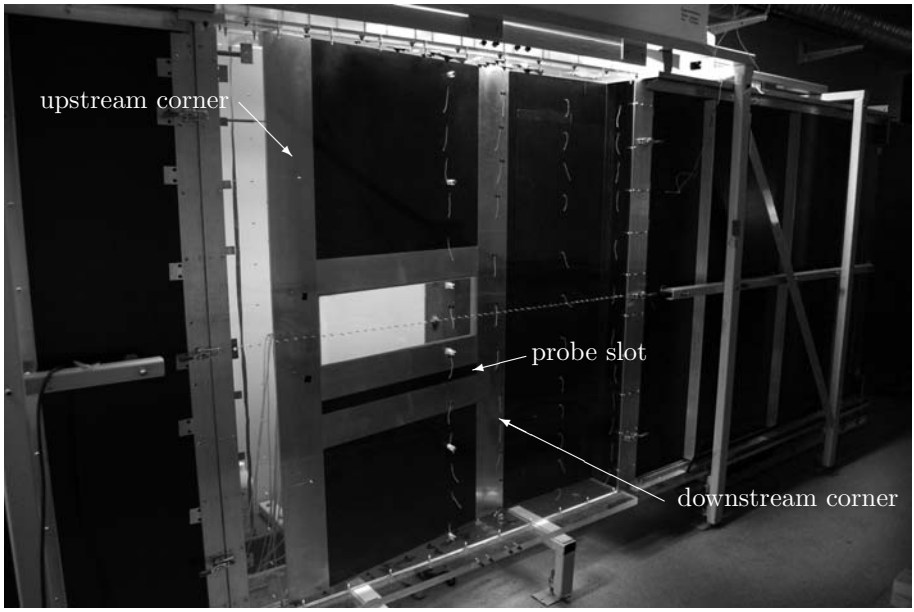

FIGURE 5. Photograph of the measurement section, the flow direction is from left to right.

wall. The space between the middle and the lower horizontal beams is intended to be used as a probe slot for measurements of *e.g.* wall shear stresses. The large dark coloured wall-parts visible in figure 5 are plywood. Two hatches allowing for access to the measurement section are located downstream the downstream corner.

When the turbulent channel flow develops in the 3 m long inlet channel boundary layers will form on the channel end walls. These boundary layers will decrease the level of momentum in a region near the end walls, making the end wall flow sensitive to adverse pressure gradients. By reducing the thickness of the end wall boundary layers through suction before the diffuser where the adverse pressure gradient starts, end wall separation can be avoided. The suction is applied through a 100 mm long perforated section of the end wall ending 50 mm before the diffuser starts. The suction is produced by a separate fan connected to the perforated parts through hoses. The air that is sucked out is brought back to the wind-tunnel circuit by leading the exit of the fan to a connection on the return channel. After the perforated section a new boundary layer will start to grow and to prevent this boundary layer from separating small vortex generators are put on the end walls in the diffuser.

A row of 57 pressure taps were drilled along the centreline of the plane wall, the distance between the pressure taps is 25 mm and the holes which are

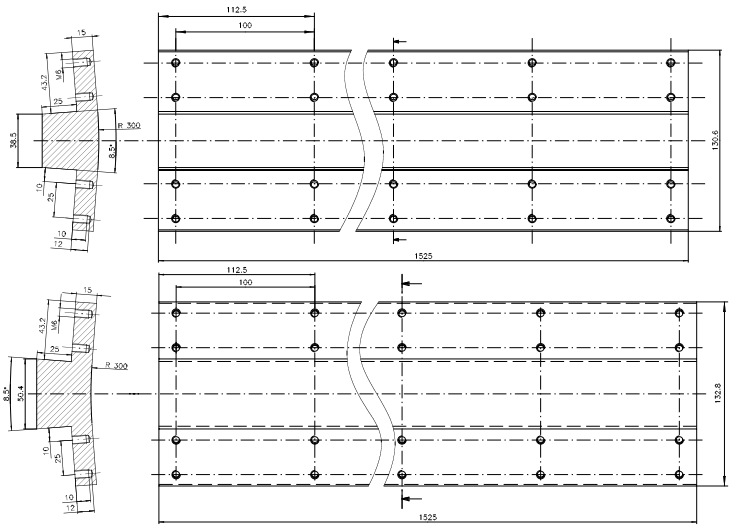

FIGURE 6. Drafts of the up- and downstream corner beams.

drilled directly in the Plexiglas® has a diameter of 0.4 mm. Similarly a coarser row of pressure holes were drilled on the opposite side of the diffuser, along the inclined wall. Pressure taps were also drilled in spanwise rows on both walls 100 mm before the upper corner of the diffuser in order to measure the spanwise homogeneity of the incoming flow.

2.6. *Exit channel and transformer before the heat exchanger*

The exit channel is built in plywood in a similar way as the inlet channel and has the purpose of reducing the effects of the downstream wind-tunnel parts on the flow in the measurement section. The size of the exit channel is $2000\times1525\times141$ mm^3 and stiffening aluminium L-profiles and adjustment screws along the centreline are used, in the same fashion as for the inlet channel, to ensure that these dimensions are kept. An open slot at the downstream end of the exit channel ensure a point in the wind-tunnel circuit with a constant reference pressure (the pressure in the laboratory) and thus avoid pulsating pressures from appearing. The slot also ensures that the pressure inside the measurement section is close to that outside of it, minimising the possibility to have an altered flow geometry due to bulging of the large Plexiglas®-window that constitutes the straight wall.

The exit channel is followed by a transformer, changing the cross section to 400×300 mm^2 in order fit the dimensions of the following heat exchanger. The shape of the contraction was determined using the same formula as for the contraction upstream the inlet channel (see section 2.4). Since the transformer

is contracting in one direction and expanding in the other the total contraction ratio is only 1.8, smaller than what one can conceive from figure 2. The sides of the transformer were sawed into the proper shape from a 25 mm thick plywood sheet and the (bent) upper and lower walls were made by steel tinplates nailed to the plywood.

2.7. *Heat exchanger and return channel*

When running the wind-tunnel, the fan is constantly adding kinetic energy to the 'closed' system. Energy which through viscous dissipation eventually will become heat. This heat has to be removed at the same rate as it is added if a constant flow temperature is desired in the experiment. In order to do so a heat exchanger, consisting of a car radiator (VW Golf II), was built into the wind-tunnel circuit. In the heat exchanger the cooling medium is tap water. No automatic temperature control system has been implemented as the temperature variations proved to be small enough for optical measurement techniques without automatic control.

After the heat exchanger the cross section shape is gradually changed from rectangular to circular with 400 mm diameter. This is done in a 650 mm long transformer section manufactured in glass fibre reinforced epoxy moulded on a plug which was formed from a block of styrofoam using a hot-wire saw.

The return channel is made of standard 400 mm diameter ventilation pipes and standard 90° bends. The total length of the return channel is approximately 12 m and five 90° bends were used. The return channel is supported by consoles bolted to the ceiling. The last bend of the return channel has two connectors for hoses one for introducing seeding particles and one for returning the air from the boundary layer suction (see section 2.5).

3. Flow quality

The wind-tunnel was first built without the return channel and preliminary tests were performed, with the aim to evaluate the inflow conditions and the two-dimensionality of the flow. Yarn tufts were used to visualise the flow direction and to convince us that no large separation was occurring on the diffuser end walls.

3.1. *Spanwise homogeneity of the inlet flow*

Pitot tube measurements of inlet flow were performed at six different spanwise positions 100 mm upstream of the first corner of the diffuser in order to evaluate the spanwise homogeneity of the inflow. In order to reduce the perturbation of the flow, the pitot tube was positioned at the end of a long carbon fibre reinforced sting (see figure 7). The pitot tube was traversed from the wall towards the channel centre with a DC servo controlled motor operated from a computer. In order to measure from the opposite wall the sting had to be

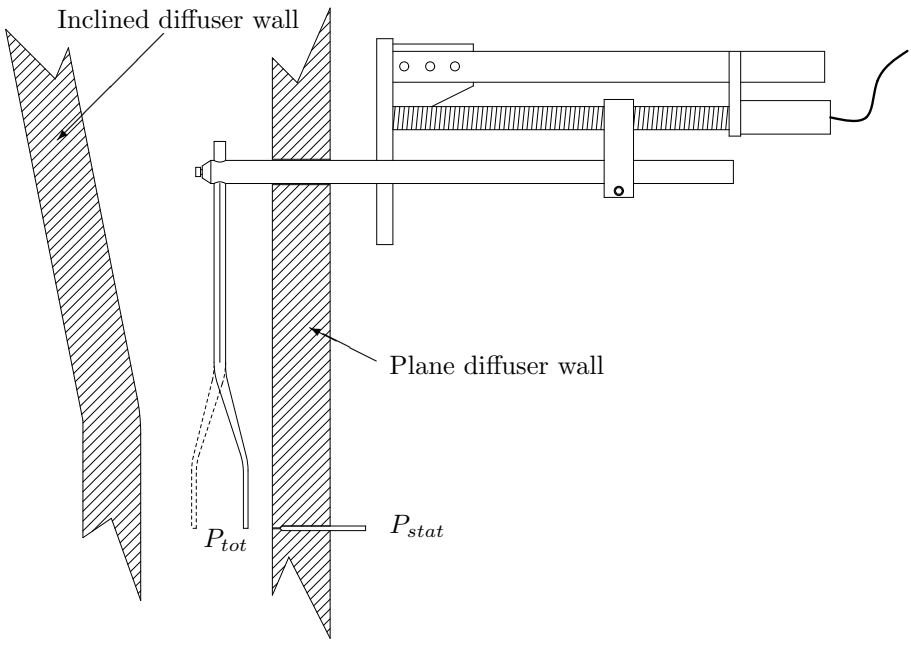

FIGURE 7. Sketch of the setup used for the pitot-tube measurements.

rotated 180° around its axis. The static pressure was measured in a hole on the plane wall and the pressure difference was measured with a Furness Control FCO 510 differential pressure transducer with an accuracy of 0.25% of full scale (2000 Pa). The measured centreline velocities were found to be constant within ±0.9% over the whole spanwise width.

3.2. *Two-dimensionality*

The previous section concerned the spanwise homogeneity of the inflow but the largest difficulty of this experiment is to get a two-dimensional flow in the adverse pressure gradient region in the diffuser. The methods used to prevent end wall separation are described in 2.5. In order to see if the end wall flow really is attached tufts taped to the end walls were used. With the boundary layer suction turned on, the only backflow that could be observed on the end walls was in the regions where the 'desired' separation is located *i.e.* near the downstream half of the inclined wall and on a limited area downstream of that. Notable is that if the boundary layer suction was turned off, a very large separated region, which was visualized with smoke, formed. This separation could extend 1/3 of the spanwise width from the end walls towards the centre line and would probably give rise to a significant flow rate increase in the downstream parts of the diffuser if measurements were taken along the diffuser centreline.

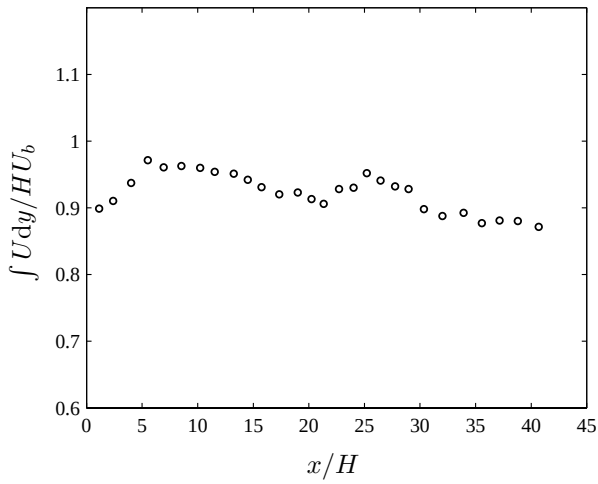

FIGURE 8. Flow rate measured with PIV.

Furthermore, the three-dimensional separation appeared to be stationary on either wall but could be forced to switch side by partially blocking of the flow coming out from the exit channel.

The flow-rate is a good measure of the two-dimensionality of a flow and for this flow a suitable definition of the flow rate is

$$\frac{1}{HU_b}\int U(y)\mathrm{d}y. \tag{7}$$

Where U is the velocity in the x-direction, H is the inlet channel height and U_b is the bulk velocity of the inlet channel flow (*i.e.* $U_b = \int U_{inlet}\mathrm{d}y/H$). Figure 8 shows the flow rate measured with PIV (see Törnblom *et al.* (2006)) in the centre region of the measurement section. The integrals of the PIV profiles are consequently smaller than the bulk flow predicted from the inlet centreline velocity and Dean's relation. The reason for this could be the lack of near wall points in the PIV-data leading to an underestimation of the integrals. More important however, is it that the data shows no trend towards increasing flow rate with increasing x-position. Such a trend would be an indication of an undesired three-dimensional separation.

3.3. *Fan speed control*

It was noticed when the first measurements with LDV were taken that the mean values of the measured velocity converged very slowly indicating some very long timescale variation, or drift, of the velocity. In order to handle this problem a LabView program was built, allowing the fan to be controlled from the computer. The LabView program measures the air temperature in the

wind-tunnel with a PT-100 temperature sensor, the friction velocity at the inlet with a Preston tube connected to a Furness Control FCO 510 differential pressure transducer and the ambient pressure with an absolute pressure transducer connected to the FCO 510. From the measured data the density and viscosity of the air is calculated. These values are used to calculate the friction velocity at the inlet and a proportional controller adjusts the fan speed to keep the friction velocity at a constant level.

4. Stereoscopic PIV measurements

4.1. *Stereoscopic setup*

The setup for the stereoscopic measurements reported in Törnblom *et al.* (2006) is shown in figure 9. The two cameras and the laser were mounted on a translation stage in order to be able to cover the whole measurement section without changing their relative positions. The translation stage was an Isel LF6, the working length was 2000 millimetre and the position repeatability is stated by the manufacturer to be 0.02 millimetres. A rig of X-95 profiles and FLS-95 rails from Linos were used to mount the cameras and the laser on the translation stage.

Two Photron Ultima APX-RS cameras were used in the setup. The resolution of the cameras' 10 bit grayscale CMOS sensors are 1024×1024 pixels and the maximum frame rate at this resolution is 3 kHz. If the image resolution is reduced it is possible to increase the frame rate up to 250 kHz. The size of the image sensors are 17.9×17.9 mm^2. The internal memory of each camera can store up to 6144 full size images which have to be transferred through a firewire interface to a PC before a new recording can be made.

The laser light sheet was formed using optics mounted directly at the laser head. The sheet optics from LaVision have three lenses, first is a fixed spherical lens with negative focal length, second is a spherical lens with positive focal length whose position is adjustable and last is a fixed cylindrical lens with negative focal length. The position of the middle lens can be altered by turning a focus ring, allowing the position of the beam waist to be adjusted between approximately 0.3 and 2.0 meters. Due to the relatively short distance between the laser and the measurement region following from the experimental setup (see figure 9) a rapidly diverging light sheet is needed in order to illuminate the whole imaged area. Thus, a cylindrical lens with a focal length of -3 millimetres was used.

The thickness of the laser light-sheet was determined by measuring the width of the correlation peaks in the cross correlation between particle images taken at the same time instant by the two cameras (Wieneke 2005). Figure 10 shows how particles, in the light sheet, that will appear at the same position in images of camera 1 will appear at different positions in the images of camera 2 (and vice versa). Therefore the correlation peaks will be smeared out in one

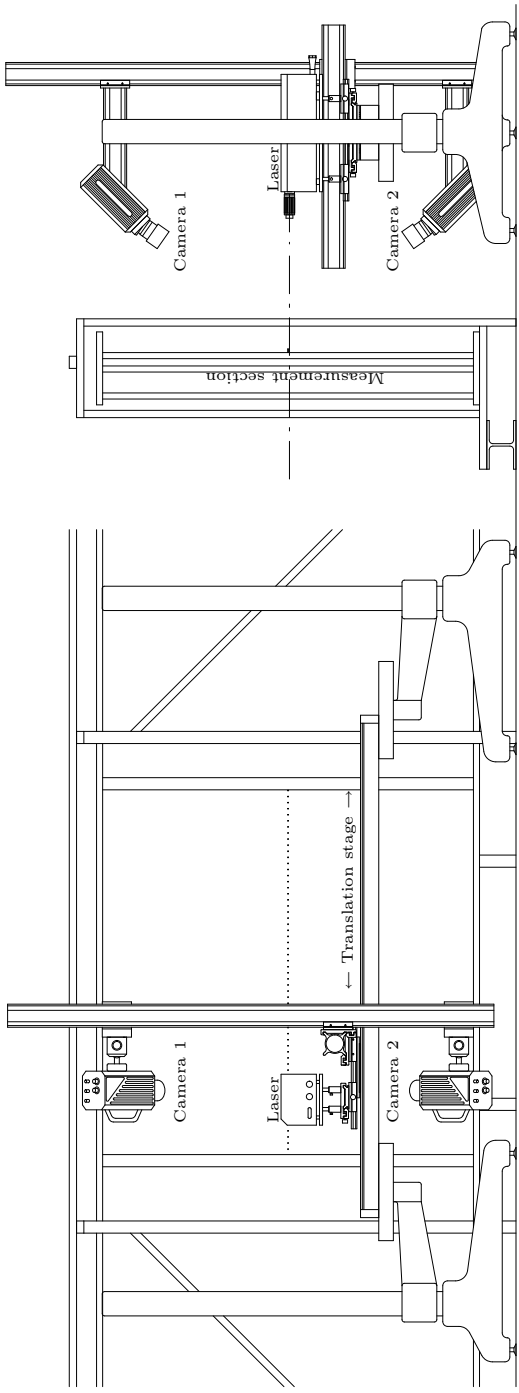

FIGURE 9. Setup for the stereoscopic PIV measurements.

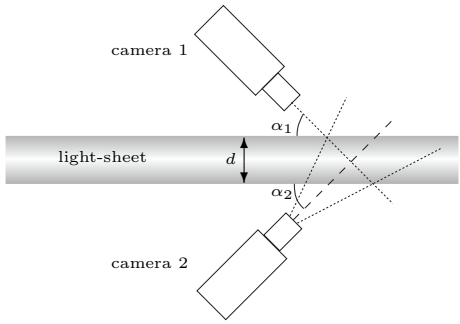

FIGURE 10. Sketch showing the reason for the smearing of correlation peaks and how the peak-width can be related to the light-sheet thickness.

direction. By simple geometrical arguments, the width W_{peak} of the correlation peaks can be related to the light-sheet thickness d according to

$$W_{peak} \approx d\left(\frac{1}{\tan(\alpha_1)} + \frac{1}{\tan(\alpha_2)}\right). \tag{8}$$

The definition of the angles α_1 and α_2 can be seen in figure 10. Using this relation, the average light sheet thickness in the experiment, was estimated to 1.5 mm.

The laser used was a New Wave Pegasus Nd:YLF with dual laser heads. Each laser head can emit up to 10000 pulses per second. The energy in each pulse is dependent on the operating frequency and the maximum is 10 mJ at a rate of 1 kHz. The laser head weighs 12 kg and was small enough to be placed on the translation stage.

4.2. *Flow seeding*

The air was seeded with smoke from a smoke-generator ZR12-AL from Jem using a mixture of glycerol and water. By varying the amount of water the density of the smoke can be optimized to give good results. The smoke was inserted just upstream of the fan and was sufficiently spread out in the measurement section due to the mixing in the fan and in the inlet channel. An estimate of the particle size based on recorded particle images and using relations for the Airy pattern given in Raffel *et al.* (1997), gave that the particles are approximately 3 μm in diameter, which is in good agreement with previous investigations of the same type of smoke.

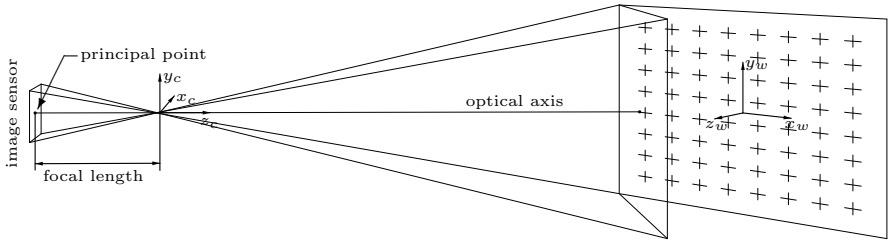

FIGURE 11. Camera pinhole model.

4.3. *Stereoscopic calibration*

In order to correctly compute a three component velocity field from the camera images it is necessary to know how the points on each camera's image sensor are related to a common 'world' coordinate system in the measurement region.

There are a few different methods to approximate the mapping functions which are used in stereoscopic PIV e.g. polynomial fitting and the camera pinhole model. For the current investigation the camera pinhole model was chosen, the reason for choosing this model was mainly because it allows for post calibration misalignment corrections, i.e. misalignment between the calibration plate and the actual position of the light sheet, by performing a 'self-calibration' on the recorded images. Another advantage of the pinhole model, as compared to polynomial fitting, is that it allows a small degree of extrapolation of the mapping function, this is important in the present flow case which is bounded by two walls making it hard to have calibration plate markers all the way out to the boundaries. Furthermore, the risk of fitting noise to the mapping function, due to imperfect detection of the calibration plate markers, is larger for the polynomial fit, since this model has about four times as many free parameters as the pinhole model. Polynomial fitting can however be advantageous in situations with large image distortions, where the pinhole model is known to suffer from convergence problems (Wieneke 2005). It should perhaps be emphasised that the chosen method is a calibration-based three-dimensional volume mapping method, not to confuse with purely geometrical ray-tracing methods which require very accurate knowledge about the experimental geometry. The software DaVis 7.0 and 7.1 by LaVision GmbH was used for the calibration.

The camera pinhole model and the self-calibration method is described in detail in Wieneke (2005). The pinhole model is based on simple geometrical relations, see figure 11, and corrections for image distortions. The world coordinate system $\mathbf{x}_w = (x_w, y_w, z_w)$, which is common for both cameras, is related to the each camera's coordinate system $\mathbf{x}_c = (x_c, y_c, z_c)$ according to

$$\mathbf{x}_c = \mathbf{R}\mathbf{x}_w + \mathbf{t}, \tag{9}$$

where $\mathbf{R}$ is a rotation matrix and $\mathbf{t}$ a translation vector. The relation between the camera coordinate system and the uncorrected image plane system $\mathbf{x}_i^{uc} = (x_i^{uc}, y_i^{uc})$, with its origin at the principal point, is then given by

$$\mathbf{x}_i^{uc} = \frac{f}{z_c}[x_c, y_c], \tag{10}$$

where f is the focal length. Last a correction for first and second order radial lens distortions is made so that image plane coordinates are

$$\mathbf{x}_i = \mathbf{x}_i^{uc}\left(1 + k_1|\mathbf{x}_i^{uc}| + k_2|\mathbf{x}_i^{uc}|^2\right), \tag{11}$$

where k_1 and k_2 are model parameters.

There are hence eleven parameters that should be fitted for each one of the cameras, i.e. the outer parameters which are three Euler angles to form $\mathbf{R}$ and the three lengths in $\mathbf{t}$ and the inner parameters; two values for the principal point, the focal length and the two parameters in the correction for radial distortions. The parameters are fitted in an interactive and iterative fashion using algorithms built into the commercial software DaVis. While fitting the parameters the user can set probable initial values and keep some parameters fixed while fitting others.

Images of a calibration plate were taken for three different z_w-positions centred around the anticipated light-sheet position. The calibration plate, see figures 12 and 13, consisted of an overhead film with printed markers fitted between two plexi-glass plates. The position of the calibration plate was changed in steps of one millimeter using a DC servo-motor translation stage.

In the present diffuser experiment it was not possible to calibrate the setup with a calibration plate at each measurement position due to limited access to the measurement section. Instead, at the beginning of a measurement the setup was calibrated in the wider exit channel of the diffuser, where it was possible to fit in a calibration plate. Then the whole setup was traversed to the position where the measurements should be taken. At this position a new calibration was performed using the self-calibration method described in Wieneke (2005).

The the self-calibration is based on cross-correlations between particle-images taken by the two cameras at the same time instant. The method allows for correction of misalignment between the calibration plate position and the actual position of the light sheet. It is also possible to correct for small relative displacements between the cameras. If the alignment between the world coordinate system and the light-sheet is perfect the cross correlation should result in zero centered correlation peaks, but if there is a displacement, such as in figure 14, it will result in a field of disparity vectors. Assuming a planar light-sheet it is then possible to calculate, using the disparity vectors, how the world coordinates should be rotated and translated in order to align the light-sheet plane. In the present experiment the disparity vector field was taken as the average of the correlation between 22 different image pairs.

FIGURE 12. The translation stage and calibration plate setup used for the stereoscopic calibration.

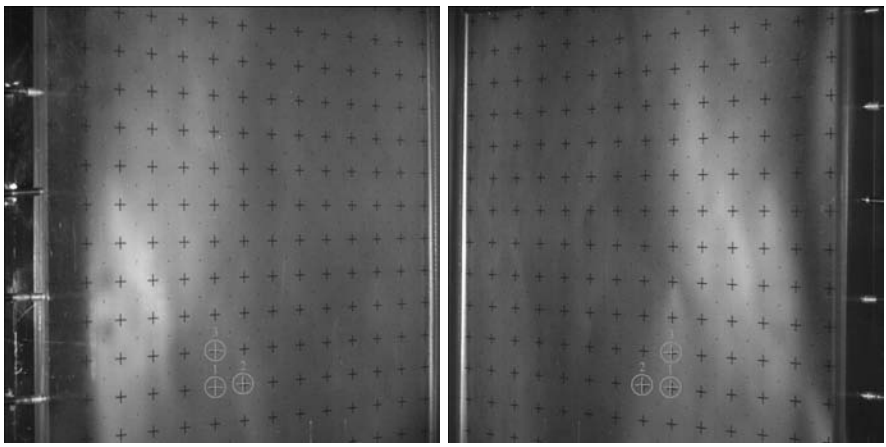

FIGURE 13. Images used for the calibration. The left image was recorded by the upper camera and the right by the lower, c.f. figure 9. The markers seen in the images are used as starting points for the marker search algorithms and for defining the world coordinates.

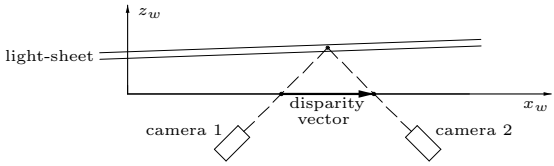

FIGURE 14. Disparity between the two cameras' images of a particle in the case of a laser-sheet and world coordinate system mismatch.

4.4. *Vector computation and image pre-processing*

Image a) in figure 15 shows a negative raw image taken directly from the camera. It can be seen that the light intensity is varying over the image due to reflections in the inclined wall, e.g. seen as darker band in the center of the channel, and the walls are so bright that the image sensor has been saturated. Tests showed that the best way to remove wall reflections and smooth out intensity variations was to subtract a temporal sliding average from the images. In the present experiment the temporal sliding average was derived from five, in the time series, consecutive images centered around the processed image. The result from the average subtraction is shown in image b) of figure 15. It can be seen that the wall reflections have been substantially diminished and that the particles are appearing more clearly.

The stereoscopic velocity vector fields are calculated using multi-pass cross-correlation where the first pass is performed with 64×64 pixel interrogation areas followed by two passes with 32×32 pixel areas, the interrogation areas are 50 percent overlapping. Before the cross-correlation is computed the images are dewarped according to the calibration mapping function and deformed according to the displacement field determined in previous passes, the method is similar to that of Scarano & Riethmuller (2000). Each one of the two image pairs gives two in-plane velocity components, these four components are combined to form a three component velocity field. The fact that four components are used to compute three is utilized to detect spurious vectors by demanding that the in-plane components of the computed three component field should not deviate more than 0.5 pixels from any of the two two-component fields. Spurious vectors are detected, removed and possibly replaced, using a four stage iterative median filter.

Step 1: Compute the median velocity in each direction for the eight surrounding vectors. Compute the standard deviation, in each direction, of the surrounding vectors, using the medians and disregarding the two velocities that deviate the most. Check, whether the components of the centre vector fulfils the requirement that they should not deviate from

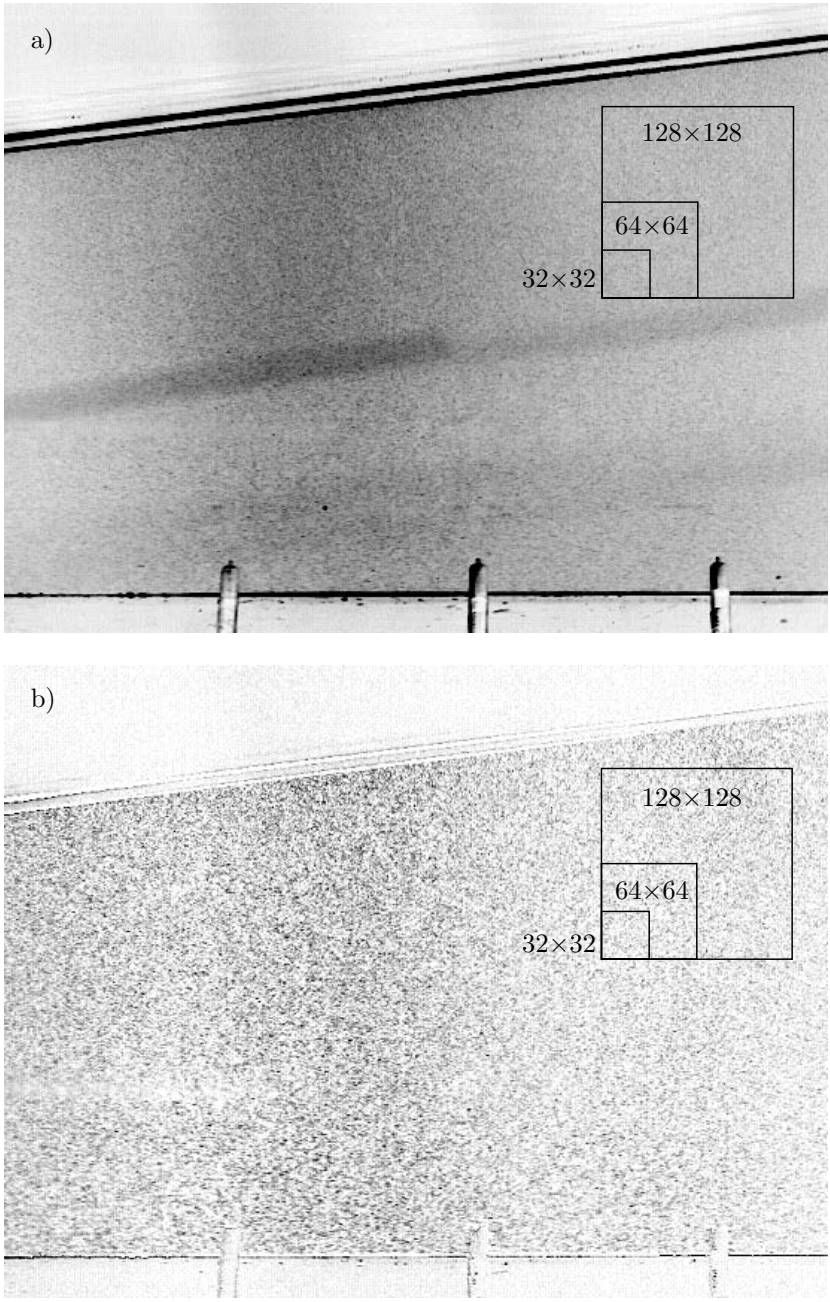

FIGURE 15. Examples of PIV-images, a) shows the unprocessed raw image and b) the image after subtraction of a temporal sliding average. The images are shown as negatives.

the median by more than a factor 2 times the standard deviation of the surrounding vectors and discard the vector if any component does not.

Step 2: Discard vectors with less than 4 neighbours.

Step 3: Fill in vectors that satisfies the requirement of not deviating more than a factor 2.5 times the standard deviation of the neighbouring vectors. The standard deviation is computed in the same way as in step 1. If the velocity given by the highest correlation peak does not satisfy the criterion the second, third and forth correlation peaks are successively tested.

Step 4: Discard any groups containing less than 5 vectors.

This method is applied to both the intermediate fields in the multi-pass processing and to the final vector-fields.

4.5. *Sources of errors in PIV*

The error level of a statistical quantity acquired with the PIV-technique will depend on contributions from a number of sources. Westerweel (1997) gives a theoretical basis for two-dimensional digital PIV, but most relations applies also to stereoscopic PIV. A typical value for the measurement error in digital PIV with 32×32 pixel interrogation areas is 0.05 to 0.1 pixel (Westerweel 1997), given that the measurement conditions fulfil a number of criteria. In the forthcoming sections these conditions and criteria are discussed in conjunction with the present experiment.

First of all, it is necessary that the particles are able to follow the flow and hence work as indicators of the velocity. Assuming Stokes drag, the relaxation time for a particle exposed to a sudden flow velocity change can be approximated as (Raffel *et al.* 1997),

$$\tau_s = \frac{d_p^2 \rho_p}{18\mu}, \tag{12}$$

where d_p and ρ_p are the particle diameter and density and μ is the dynamic viscosity of the fluid. Assuming the particle size to be 3 μm one finds the particle response time to be of the same order of magnitude as the Kolmogorov timescale in the inlet channel. This rough estimate give support for the underlying assumption that the air motion can be detected in the particle displacements.

PIV random error sources can *e.g.* be noise which can come from background disturbances, refections, poor image contrast or resolution. By careful design of the experiment these types of errors can be kept small. The background disturbances in the present experiment were kept small by having, wherever it was feasible, a dull black background in the images. Wall reflections were in some cases unavoidable in the present experiment and areas where the measurements could be affected by this was masked before the vector calculations begun. Image contrast was optimized within the restrictions posed by the

available laser power by running the laser at a repetition rate close to where the pulse energy is maximal.

4.5.1. *Loss of particle pairs*

Particles that move into, or out of, the light-sheet, often referred to as loss of pairs, are adding noise to the correlation but may also give a bias if the average velocity perpendicular to the light sheet is nonzero or if there is a nonzero turbulence correlation (*i.e.* Reynolds stress) between the velocity component perpendicular to the light sheet and a velocity component in the plane of the light sheet. Errors related to loss of pairs can be controlled by adjusting the light sheet thickness and the time between the images. Keane & Adrian (1990) showed that the influence of this type of error was small as long as the relation

$$\frac{|W|\Delta t}{\Delta z} < 0.25, \tag{13}$$

between the cross-plane velocity W, the time between frames Δt and the light-sheet width Δz, is fulfilled.

The perhaps most important condition to meet in order to have a good signal to noise relation is that the particle density should be high enough, Keane & Adrian (1992) recommends that at least seven particle pairs should appear in both interrogation areas, which requires at least ten particle images in each interrogation area if the loss of pairs due to motion out of the light-sheet is kept within the limits given by equation 13.

In the present experiment the cross-plane average velocity is zero and no turbulence correlations exists between the in-plane and cross-plane velocities. The maximum turbulent velocity w_{rms} that was measured was $\sim$1.3 m/s, at that measurement position $\Delta t = 100$ μs which together with $\Delta z = 1.5$ mm means that more than 99% of the samples should be within the limits given by equation 13 if the probability distribution is Gaussian. Furthermore, it was made sure in all measurements that the number of particles per interrogation area was sufficient.

Another way in which pairs are lost is when particles are moving into or out from the interrogation area due to in plane motions. A remedy for this problem is to shift the interrogation areas an integer number of pixels, according to an estimate of the local velocity, so that the expected displacement measured by the cross-correlation is between 0 and 0.5 pixels. By shifting the interrogation areas another problem is also resolved, the bias towards lower velocities due to the diminishing interrogation area overlap with increasing displacement. The latter problem can also be completely resolved by dividing the computed correlation with the convolution of the interrogation windows (Westerweel 1997). However, if window shifting is used, this type of weighting of the correlations is in general not necessary since the absolute error due to this bias is very small for displacements between 0 and 0.5 pixels. The method

used in the present investigation uses interpolation to perform window shifting by fractions of pixels and no weighting was applied to the correlation.

4.5.2. *Velocity gradients*

A velocity gradient over an interrogation area will give rise a broader and lower correlation peak and hence a decreased signal to noise ratio. The broadening of the peak will also make it more susceptible to the type of bias, which is due to the diminishing interrogation area overlap with increasing displacement. The bias problem can, as described above, be resolved by window shifting or weighting but the widening of the peak may decrease the accuracy in the prediction of its center and noise will have a larger influence on the peak shape. Keane & Adrian (1990) and Westerweel (1997) recommends that the rule of thumb

$$\frac{|\Delta U|\Delta t}{S} < 0.03 - 0.05, \tag{14}$$

should be followed in order to maintain a decent signal to noise ratio and hence a low measurement uncertainty. ΔU and S in the above equation are the velocity variation over the interrogation area and the physical size of the interrogation area respectively. It should also be noted that smaller interrogation areas are less sensitive to velocity gradients than larger (Raffel *et al.* 1997). The DaVis 7.1 software used in the present investigation uses a window deformation method similar to that presented in Scarano & Riethmuller (2000) to increase the signal to noise ratio. The method utilizes the velocity fields from the multi-pass evaluation not only to translate the interrogation areas but also, by image interpolation, to rotate and deform them, this is shown by Scarano & Riethmuller to both reduce noise at small velocity gradients and also allow measurements in a greater range of velocity gradients as compared to traditional methods.

4.5.3. *Peak-locking*

A specific problem in PIV when using digital images is the so called peak-locking. Peak-locking is the tendency towards integer particle displacement predictions. The most important factor influencing peak-locking is the particle image diameter. Raffel *et al.* (1997) shows that the optimum diameter for cross-correlation PIV is 2–3 pixels, if the diameter is too small the bias due to peak-locking is dominating the measurement error and if it is too large random errors will have an increased influence on the displacement predictions. The choice of sub-pixel interpolation method used in determining the correlation peak position will also influence the peak-locking errors, *e.g.* Westerweel (1997) shows that a Gaussian peak fit is superior to a peak centroid in this aspect. The window deformation method introduced by Scarano & Riethmuller (2000), which uses a non-integer interrogation area shift, was shown to efficiently remove peak-locking in an experiment where the particle image diameter was 1.6

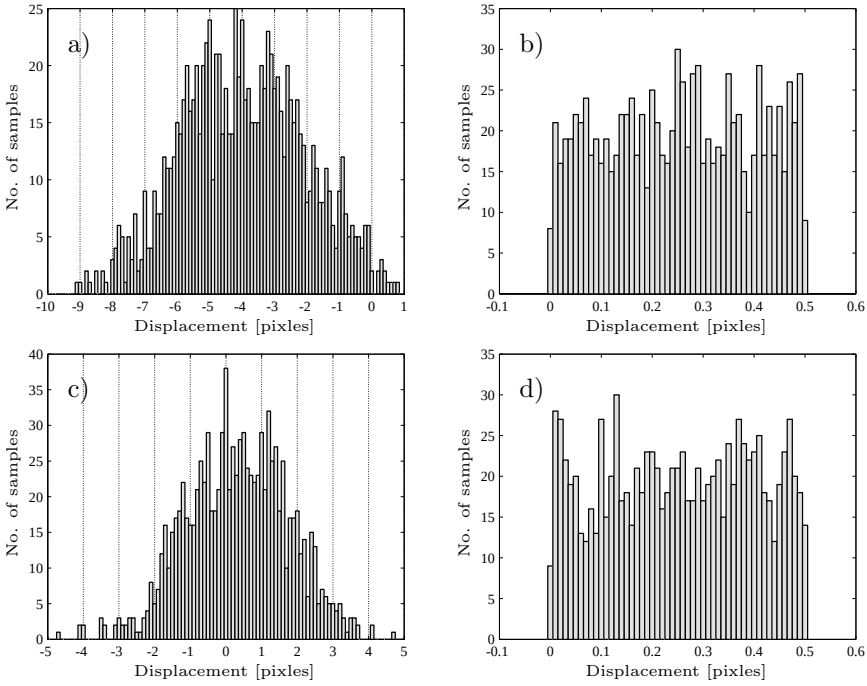

FIGURE 16. Histograms of pixel displacements samples from one point, a) streamwise component (U), b) mod(U,0.5), c) wall-normal component (V), d) mod(V,0.5).

pixels. The particle image size in the present investigation is estimated to be approximately two pixels. Figure 16 shows histograms of the velocities measured at $x \approx 25$ and $y \approx 2.5$, the histograms were taken from cross-correlations of images from a single camera so that smearing of any peak-lock errors due to the three component recombination is avoided. The modulus after division of the displacements with 0.5 is also shown in figure 16, this quantity gives a good indication of the amount of peak-locking that is in the data, with a large ratio of peak-locked samples the modulus is shifted towards zero and with no peak-locking the modulus should be evenly spread out over the interval. The conclusion drawn from figure 16 is that it is reasonable to assume that the peak-locking errors of the measurements are small.

4.5.4. *Stereoscopic errors*

In the present stereoscopic setup the measured displacements in the x, y and z directions are approximately given by

$$\begin{aligned} \Delta x &\approx \frac{\Delta x_1 + \Delta x_2}{2} \\ \Delta y &\approx \frac{\Delta y_1 + \Delta y_2}{2\cos 30^\circ} \\ \Delta z &\approx \frac{\Delta y_2 - \Delta y_1}{2\sin 30^\circ}, \end{aligned} \tag{15}$$

respectively. Indices in the above relations refer to the two cameras and 30° is the angle between the cameras' optical axes and the measurement plane normal. Assuming that the uncertainty of the measured displacements in each image is the same in both directions and that it has the standard deviation ϵ_{rms} results in the following root mean square uncertainties in the displacements:

$$\begin{aligned} \Delta x_{rms} &\approx \frac{\epsilon_{rms}}{\sqrt{2}} \approx 0.7\epsilon_{rms} \\ \Delta y_{rms} &\approx \frac{\epsilon_{rms}}{\sqrt{2}\cos 30^\circ} \approx 0.8\epsilon_{rms} \\ \Delta z_{rms} &\approx \frac{\epsilon_{rms}}{\sqrt{2}\sin 30^\circ} \approx 1.4\epsilon_{rms}. \end{aligned} \tag{16}$$

This means that the precision of the measured in-plane velocities will be slightly better as compared to non-stereoscopic PIV measurements and that the out of plane component will have an uncertainty which is roughly twice that of the other components.

Imperfection in the stereoscopic setup and calibration, such as misalignment between the calibration plate and the light sheet, may introduce considerable errors. Such misalignments will result in a mismatch between the particle images of the two cameras when these are mapped to the measurement plane, the size of this mismatch, δx, is sometimes called registration error. Van Doorne (2004) points out that

$$\left|\frac{\partial U}{\partial x}\right| \Delta t \delta x \ll 0.1 \quad \text{pixel} \tag{17}$$

in order for the for the measurement error not to be dominated by the registration errors.

The self-calibration method used in the present investigation ensure that δx<0.1 pixel and the maximum Δt in the measurements was 100 μs, thus $|\partial U/\partial x|$ must be $\ll 10^4$ for equation 17 to be satisfied. This requirement corresponds to the requirement that the distance between two consecutive points in a velocity profile of figure 17 should be $\ll 6.4H$, so equation 17 can be considered fulfilled for all points in figure 17. The points in the first four or

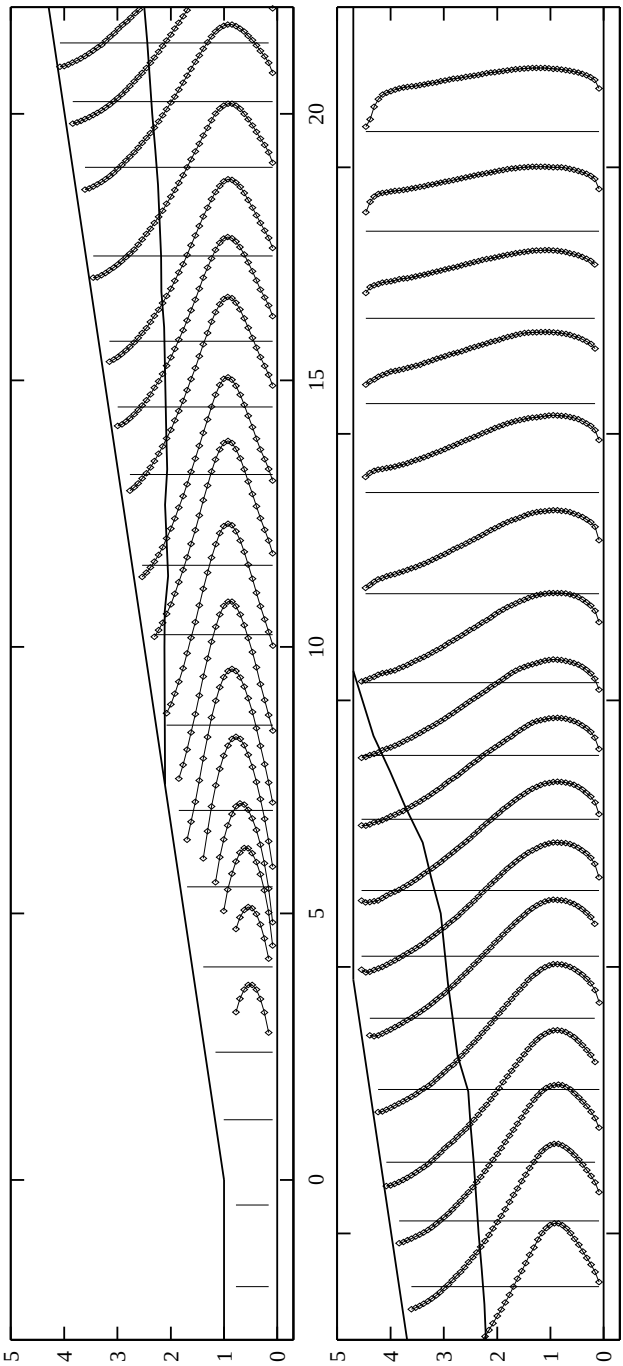

FIGURE 17. Streamwise mean velocity, ($U_{\text{fig}} = 5U/U_b + x/H$). The vertical lines indicate zero level for each streamwise velocity profile and a solid contour indicates the path of the dividing streamline.

five profiles in the diffuser were measured with a Δt of 50–70 μs so here the requirement is instead that the distance should be $\ll 9 - 12.8H$.

4.5.5. *Spatial filtering*

A velocity vector, measured with two-dimensional PIV, will be the average velocity in a measurement volume constituted by the thickness of the light-sheet and the dimensions of the interrogation area. This averaging will, if the size of the measurement volume is larger than the smallest scales of the turbulent flow, result in a spatial low-pass filtering of the velocity field. Measured mean velocities are not affected by the spatial filtering, but the measured second order statistics will be biased towards lower values since the energy residing in the high wave-number part of the turbulence spectrum will be filtered away.

In stereoscopic PIV the measurement volume will be larger than the interrogation areas in one of the in-plane directions due to the oblique viewing. In the present setup, the measurement volumes are elongated in the y-direction. A comparison of the second order turbulence statistics measured in the present stereoscopic setup with finer resolved two-component measurements revealed that the stereoscopic data was biased towards lower turbulence levels due to spatial filtering.

Acknowledgements

The authors would like to thank Ulf Landén and Marcus Gällstedt for aiding in the manufacturing of the wind-tunnel and measurement equipment. The Swedish Research Council and The Swedish Energy Agency are gratefully acknowledged for their financial support.

References

Angele, K. P. & Muhammad-Klingmann, B. 2005 PIV measurements in a weakly separating and reattaching turbulent boundary layer. *Eur. J. Mech. B/Fluids* **25**, 204–222.

Buice, C. U. & Eaton, J. K. 1997 Experimental investigation of flow through an asymmetric plane diffuser. *Tech. Rep.*. Department of mechanical engineering, Stanford university.

Cherry, N. J., Hillier, R. & Latour, M. E. M. P. 1984 Unsteady measurements in a separated and reattaching flow. *J. Fluid Mech.* **144**, 13–46.

Chithambaran, V. K., Aswatha, P. A. & Chandrasekhara Swamy, N. V. 1984 Mean velocity characteristics of plane diffuser flows with inlet velocity distortion. *J. Indian Inst, Sci.* **65(A)**, 79–93.

Comte-Bellot, G. 1965 Écoulement turbulent entre deux paroix parallèles. Publications scientifiques et techniques 419. Ministère de l'air, 2, Avenue de la Porte-d'Issy, Paris.

Dianat, M. & Castro, I. P. 1991 Turbulence in a separated boundary layer. *J. Fluid Mech.* **226**, 91–123.

van Doorne, C. W. H. 2004 Stereoscopic PIV on transition in pipe flow. PhD. Thesis, Technische Universiteit Delft, ISBN 90-9018499-6.

Etheridge, D. W. & Kemp, P. H. 1978 Measurements of turbulent flow downstream of a rearward-facing step. *J. Fluid Mech.* **86**, 545–566.

Johansson, A. V. & Alfredsson, P. H. 1982 On the structure of turbulent channel flow. *J. Fluid Mech.* **122**, 295–314.

Johansson, A. V. & Alfredsson, P. H. 1986 Structure of tubulent channel flows. In *Encyclopedia of Fluid Mechanics*, chap. 25, pp. 825–869. Gulf publishing company.

Keane, R. & Adrian, R. 1992 Theory of cross-correlation in PIV. *Applied scientific research* **49**, 191–215.

Keane, R. D. & Adrian, R. J. 1990 Optimization of particle image velocimeters. Part I; double pulsed systems. *Meas. Sci. Technol.* **1**, 1202–1215.

Laws, E. & Livesey, J. 1978 Flow through screens. *Ann. Rev. Fluid Mech.* **10**, 247–266.

Lindgren, B. & Johansson, A. V. 2002 Design and evaluation of a low-speed wind-tunnel with expanding corners. Technical report ISRNKTH/MEK/TR–02/14-SE. Dept. of mechanics, KTH.

Obi, S., Aoki, K. & Masuda, S. 1993 Experimental and computational study of turbulent separating flow in an asymmetric plane diffuser. In *Ninth Symp. on Turbulent Shear Flows*, p. 305. Kyoto, Japan.

Perry, A. E. & Fairlie, B. D. 1975 A study of turbulent boundary-layer separation and reattachment. *J. Fluid Mech.* **69**, 657–672.

Raffel, M., Willert, C. & Kompenhans, J. 1997 *Particle Image Velocimetry, A practical guide*. Springer Verlag.

Ruderich, R. & Fernholz, H. H. 1975 An experimental investigation of a turbulent shear flow with separation, reverse flow, and reattachment. *J. Fluid Mech.* **163**, 283–322.

Scarano, F. & Riethmuller, M. L. 2000 Advances in iterative multigrid piv image processing. *Exp. Fluids* **29 [Suppl.]**, S51–S60.

Sovran, G. & Klomp, E. D. 1967 Experimentally determined optimum geometries for rectelinear diffusers with rectangular, conical, or annular cross-section. In *Fluid mechanics of internal flow* (ed. G. Sovran), pp. 270–319. Elsevier publishing company.

Taylor, G. & Batchelor, G. K. 1949 The effect of wire gauze on small disturbances in a uniform stream. *Quart. J. Mech. and App. Math.* **2**, part 1,1.

Törnblom, O., Lindgren, B. & Johansson, A. V. 2006 Measurements of mean flow statistics in a plane asymmetric diffuser with 8.5° opening angle. *To be submitted* (**Paper 1**).

Westerweel, J. 1997 Fundamentals of digital particle image velocimetry. *Meas. Sci. Technol.* **8**, 1379–1392.

Wieneke, B. 2005 Stereo-PIV using self-calibration on particle images. *Exp. in Fluids* **39**, 267–280.

Yoshioka, S., Obi, S. & Masuda, S. 2001 Turbulence statistics of periodically perturbed separated flow over backward facing step. *Int. J. Heat Fluid Flow* **22**, 391–401.

TRITA-MEK
Technical Report 2006:15
ISSN 0348-467X
ISRN KTH/MEK/TR-06/15-SE
ISBN 91-7178-416-0

www.kth.se